Overview of SAX99: Environmental Considerations

Michael D. Richardson, Kevin B. Briggs, L. Dale Bibee, Peter A. Jumars, William B. Sawyer, Daniel B. Albert, Richard H. Bennett, Thomas K. Berger, Michael J. Buckingham, Nicholas P. Chotiros, Peter H. Dahl, Nancy T. Dewitt, Peter Fleischer, Roger Flood, Charles F. Greenlaw, D. Vance Holliday, Matthew H. Hulbert, Michael P. Hutnak, Peter D. Jackson, Jules S. Jaffe, H. Paul Johnson, Dawn L. Lavoie, Anthony P. Lyons, Christopher S. Martens, Duncan E. McGehee, Karl D. Moore, Tim H. Orsi, James N. Piper, Richard I. Ray, Allen H. Reed, Robert. F. Liko Self, Jill L. Schmidt, Stephen G. Schock, Fernando Simonet, Robert D. Stoll, Dajun Tang, David E. Thistle, Eric I. Thorsos, Donald J. Walter, and Robert A. Wheatcroft

***Abstract*—A 1-km^2 area located 2 km off the Florida Panhandle (30°22.6′N; 86°38.7′W) was selected as the site to conduct high-frequency acoustic seafloor penetration, sediment propagation, and bottom scattering experiments [1]. Side scan, multibeam, and normal incidence chirp acoustic surveys as well as subsequent video surveys, diver observations, and vibra coring, indicate a uniform distribution of surficial and subbottom seafloor characteristics within the area. The site, in 18–19 m of water, is characterized by 1–2–m-thick fine-to-medium clean sand and meets the logistic and scientific requirements specified for the acoustic experiments. This paper provides a preliminary summary of the meteorological, oceanographic, and seafloor conditions found during the experiments and describes the important physical and biological processes that control the spatial distribution and temporal changes in these characteristics.**

***Index Terms*—Acoustic propagation, acoustic scattering, acoustic velocity measurement, geologic measurements, marine animals, meteorology, seafloor, sediments.**

Manuscript received January 30, 2000; revised October 10, 2000.

M. D. Richardson, K. B. Briggs, L. D. Bibee, W. B. Sawyer, D. L. Lavoie, R. I. Ray, A. H. Reed, and D. J. Walter are with the Marine Geosciences Division, Naval Research Laboratory, Stennis Space Center, MS 39529-5004 USA.

P. A. Jumars is with the Darling Marine Center, University of Maine, Walpole, ME 04573-3307 USA.

D. B. Albert and C. S. Martens are with the Marine Sciences Department, University of North Carolina, Chapel Hill, NC 27599-3300 USA.

R. H. Bennett is with the SEAPROBE, Inc., Picayune, MS 39466 USA.

T. K. Berger and F. Simonet are with the Marine Physical Laboratory, Scripps Institution of Oceanography, La Jolla, CA 92093-0213 USA.

M. J. Buckingham is with the Marine Physical Laboratory, Scripps Institution of Oceanography, La Jolla, CA 92093-0213 USA and also with The Institute of Sound and Vibration Research, The University of Southampton, SO17 1BJ, U.K.

N. P. Chotiros and J. N. Piper are with the Applied Research Laboratories, University of Texas at Austin, Austin, TX 78713-8029 USA.

P. H. Dahl, D. Tang and E. I. Thorsos are with the Applied Physics Laboratory, University of Washington, Seattle, WA 98105 USA.

N. T. Dewitt is with the US Geological Survey, Center for Coastal Studies and Regional Geology, St. Petersburg, FL 33701 USA.

P. Fleischer is with the Marine Geosciences Division, Naval Research Laboratory, and the Naval Oceanographic Office, Stennis Space Center, MS 39529-5004 USA.

R. Flood is with the Marine Science Laboratory, State University of New York at Stony Brook, Stony Brook, NY 11794 USA.

C. F. Greenlaw, D. V. Holliday, and D. E. McGehee are with the Ocean Sciences Research Group, Analysis & Applied Research Division, BAE SYSTEMS, San Diego, CA 92123-4333 USA.

M. H. Hulbert is with Pittman-Moore, Inc., Terra Haute, IN 47808 USA.

M. P. Hutnak and H. P. Johnson are with the School of Oceanography, University of Washington, Seattle, WA 98195 USA.

P. D. Jackson is with the British Geological Survey, Keyworth, Nottingham, NG12 5GG UK

J. S. Jaffe and K. D. Moore are with the Scripps Institution of Oceanography, San Diego CA 92093-0208 USA.

A. P. Lyons is with the NATO SACLANT Undersea Research Centre, 19138 La Spezia, Italy.

T. H. Orsi is with Planning Systems, Inc., Slidell, LA 70658 USA.

R. F. L. Self is with the School of Oceanography/Friday Harbor Labs, University of Washington, Friday Harbor, WA 98250 USA.

J. L. Schmidt is with the Department of Oceanography, University of Washington, Seattle, WA 98195-7940 USA.

S. G. Schock is with the Department of Ocean Engineering, Florida Atlantic University, Boca Raton, FL 33431 USA.

R. D. Stoll is with the Lamont-Doherty Earth Observatory, Columbia University, Palisades, NY 10964 USA.

D. E. Thistle is with the Department of Oceanography, Florida State University, Tallahassee, FL 32306 USA.

R. A. Wheatcroft is with the Oceanic and Atmospheric Sciences, Oregon State University, Corvallis OR, 97331 USA.

Publisher Item Identifier S 0364-9059(01)01565-5.

I. Introduction

THE SAX99 (Sediment Acoustics Experiment 1999), conducted in the northeastern Gulf of Mexico during September–November 1999 (Fig. 1), is part of an Office of Naval Research (ONR) department research initiative on high-frequency sound interaction in ocean sediments. This research program addresses high-frequency acoustic penetration into, propagation within, and scattering from the shallow-water seafloor. Since the program was first initiated to study the mechanisms for high-frequency acoustic energy penetration into sediments at low grazing angles, some background on that controversial issue is given. Other acoustic scattering and propagation issues are discussed in later paragraphs.

Sound speed in sand sediment is greater than that of the overlying water. If such sediments are modeled as fluids with flat interfaces, a critical grazing angle is predicted below which there will be no appreciable acoustic penetration. There is, however, substantial evidence for penetration below this critical grazing angle, which implies that a fluid-sediment, flat-interface model is inadequate [2]–[7]. It has been theoretically shown that shear effects in sand sediments are unimportant and can be safely ignored [8]. At present, three other mechanisms are hypothesized to contribute to subcritical acoustic penetration. First, the porous nature of the sediment leads to a "slow" wave with a speed less than the of sound speed of the overlying water; thus no critical angle exists for that converted wave [2]. Second, seafloor roughness diffracts energy into the sediment [9], [10]. Third, sediment volume heterogeneity scatters the evanescent wave energy that propagates along the seafloor interface into the sediment [7].

In order to compare the predictions of penetration of high-frequency acoustic energy into sediments based on these

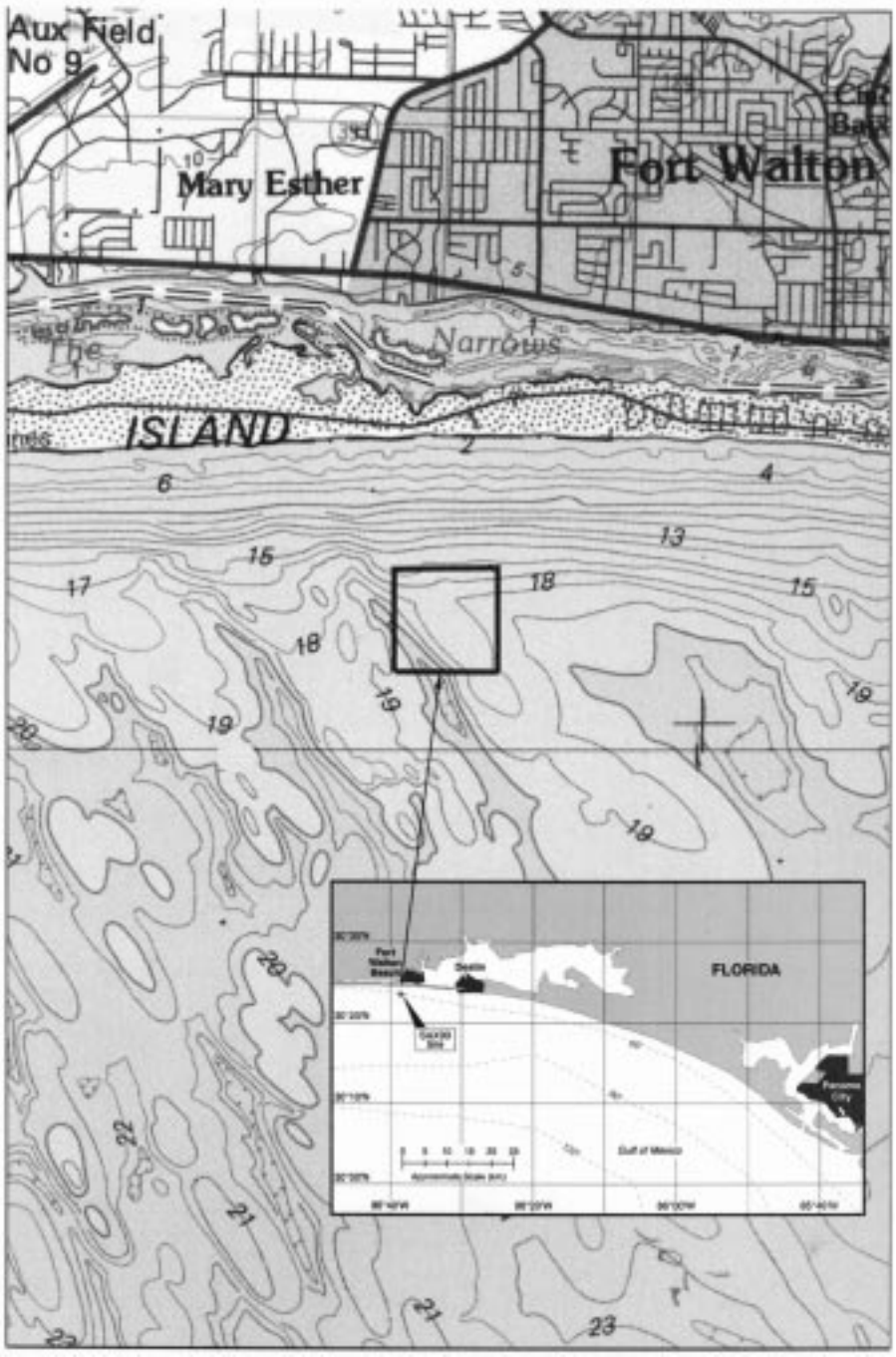

Fig. 1. Bathymetric map of the SAX99 experimental site showing the ridge topography common to the northeastern Gulf of Mexico, experimental site location, and area of acoustic surveys using side scan, multibeam, and normal incidence sonars.

three hypotheses to actual acoustic data, seafloor roughness and the spatial variability of sediment physical and geoacoustic properties must be characterized. In the past, the lack of adequate sediment characterization has allowed acoustic modelers to choose values for seafloor properties that are in concordance with their hypothesized penetration mechanism. An objective of the SAX99 experiments is to provide statistical characterization of the seafloor, which eliminates this subjective option.

A number of other fundamental acoustics issues related to high-frequency sound interaction with the seafloor are being investigated by the SAX99 experiments. The relative dominance of scattering mechanisms (interface roughness, volume heterogeneities, bubbles, sediment grains, and discrete scatterers such as shells) versus frequency and/or sediment type is not well known [11]. Experiments, including those that manipulate the environment, are needed to isolate scattering mechanisms over the frequency range of 10–500 kHz [12]. The importance of fine-scale gradients or stratification in controlling scattering needs to be better understood [13]. The importance of multiple versus single point scattering also needs to be clarified [14]. A variety of fluid, suspension, elastic, visco-elastic, and poro-elastic models are used to predict acoustic propagation in unconsolidated sediments [15]–[17]. Which models are appropriate for which sediments? Which

simplifications are appropriate for prediction of acoustic scattering from the seafloor? Of particular interest are the issues of attenuation versus frequency and sound speed dispersion of acoustic waves propagating in the seafloor [18], [19]. Spatial and temporal variability in seafloor properties is common from micron to kilometer scales [20]. Are current continuum scattering and propagation models adequate? Are stochastic models required? Aspects of these and other issues are addressed simultaneously with the subcritical penetration investigations during the SAX99 experiments.

If the high-frequency acoustic bottom interaction models are to be utilized outside specific experimental conditions, the effects of environmental processes (biological, hydrodynamic, geological, and biogeochemical) on the spatial and temporal distribution of properties that control propagation, scattering, and penetration phenomena must be understood [21]. It is expected that short-term biological modification of surface roughness and long-term hydrodynamic modification of sediment morphology and roughness are the dominant environmental processes controlling seafloor properties at the SAX99 experimental site.

In this paper the site selection process is described; the meteorological, oceanographic, and seafloor conditions during the experiments (1 October through 10 November 1999) are documented; and the biological and physical processes that alter the spatial and temporal environmental conditions are presented. Because of the short time interval between the experiments and the writing of this paper data, analyzes, and interpretations presented herein should be considered preliminary. A companion paper [1] describes the actual high-frequency acoustic experiments conducted during SAX99.

A. Seafloor Requirements

Based on an evaluation of acoustic modeling requirements, values of the following sediment properties were either measured or will be determined from samples collected during the experiments.

- Sediment grain properties: grain size, distribution, shape and surface texture, grain density, bulk modulus, organic matter composition, and mineralogy.
- Water properties: density, bulk modulus, viscosity, and sound speed measured for pore fluid or calculated from pore water temperature, salinity, and pressure.
- Porometry: two- and three-dimensional porosity, tortuosity, permeability, pore size distribution and geometry, and grain size distribution, shape, and contact geometry.
- Bulk density, porosity, void ratio, and percent organic matter.
- Frame bulk and shear modulus.
- Frame bulk and shear log decrement.
- Shear and compressional speed and attenuation.
- Two-dimensional seafloor roughness (spatial and temporal variations).
- Bubble size, distribution, and volume.
- Size and distribution of discrete scatterers.

Sediment properties require different levels of measurement effort. For several properties, physical handbook determination is adequate (e.g., pore water density, bulk modulus, viscosity, and sound speed can accurately be determined from pore water temperature, salinity and pressure). Laboratory determination of sediment grain size properties is adequate, although variability and vertical gradients should be statistically quantified. Other properties such as geoacoustic (shear and compressional wave speed and attenuation) properties, seafloor roughness, and bubble characterization need to be measured *in situ*. Frame bulk and shear moduli and log decrements can be estimated from sediment geoacoustic properties or measured in laboratory conditions. Based on acoustic model requirements, mean values, range, statistical variability, vertical gradients, and statistical characterization of two- and three-dimensional spatial variability of sediment properties are required. Measurement scales required to statistically characterize the heterogeneity of many sediment properties such as bulk density, compressional wave speed and attenuation, and bottom roughness depend on acoustic frequency. Measurement scale requirements are one-quarter of an acoustic wavelength, or as small as 1 cm, for penetration experiments and as small as 1 mm for scattering experiments. Most measurements were made with existing technology, but development of specialized new techniquess was required for certain measurements (e.g., resin impregnation for the porometry; *in situ* electrical resistivity and permeability; high-frequency acoustic tomography; and microtopography using laser line scanners and digital stereo photography). Measurements included laboratory measurements on sediments carefully collected by divers, *in situ* probe measurements, photography, resin impregnation techniques and laboratory testing. These measurements cover spatial scales of tens of centimeters with *in situ* techniques, centimeter scales with coring, submillimeter scales with CT scan and other X-radiographic techniques, and micron scales with resin impregnation techniques. Bottom roughness (meter to mm scales) at appropriate spatial and temporal scales for natural and manipulative experiments was measured by stereo-photography using diver- and fixed-mounted cameras, laser line scanners, and tomography systems. The overlapping scales should provide the statistical characterization and vertical and horizontal correlation lengths required by acoustic modelers.

B. Oceanographic and Biological Requirements

Physical oceanographic and biological processes control sediment properties and often lead to strong spatial and rapid temporal changes in sediment characteristics and bottom microtopography [21], [22]. Temporal changes in profiles of salinity, temperature, and sound speed were measured with bottom-mounted and ship-deployed conductivity temperature depth (CTD) sensors. Current speed and direction were measured using bottom-mounted, upward-looking, and ship-mounted, downward-looking Acoustic Doppler Current Profilers (ADCP). Together with surface gravity wave statistics measured with a bottom-mounted pressure sensor and a wave buoy, these oceanographic data provide the basis for understanding and predicting bottom stresses that can cause bedform modification and changes to sediment characteristics. Biological processes, especially sediment reworking by larger epifauna and fish, can rapidly change bedform morphology

and sediment structure [20]. Benthic community structure (macrofaunal, meiofaunal and microfaunal composition, density and biomass) will be determined from sediment samples while video, still and time-lapse photography were used to quantify the presence and behavior of larger epifaunal and infaunal organizms. Biological processes within the water column, such as faunal emergence, can directly affect acoustic scattering in the water column and indirectly alter seafloor microtopographic by the emergence from and re-entry of fauna into the seafloor. Physical traps, exclusion experiments, and acoustic measurements were used to document the effects of faunal emergence on seafloor properties and to develop models based on ambient light conditions. Acoustic techniques can provide valuable tools to quantity biological and physical processes [22], [23]. In order to utilize acoustic techniques as a measure of rates of biological and physical processes (the inverse acoustic model), the forward acoustic propagation and scattering models must be validated by experiments (such as SAX99) that include concurrent characterization of environmental processes, sediment properties, and acoustic seafloor interactions.

II. Site Survey

The purpose of the site survey was to select a large (600×600 m) uniform area with the environmental characteristics required by the acoustic experimenters and to provide average values of seafloor properties for pre-experimental acoustic simulations. Based on critical angle requirements, sediments were required to be uniform, well-sorted, fine to medium sand without significant layering to depths of 1–2 m. The sediment should be free of vegetation, gas bubbles, and other heterogeneities such as large shells. Experimental procedures required a benign environment for diver operations and temporal stability in environmental conditions during the experiment. Water depths of 15–20 m were required as a compromise between bottom time requirements of the extensive diver operations and to minimize sea surface acoustic reflections.

Site selection included a reconnaissance cruise aboard the R/V Seward Johnson (16 August–6 September 1998); a site survey aboard the R/V Pelican (8–19 July 1999); vibracoring aboard the R/V Gilbert (18–20 March 1999; 24–29 August 1999); a multibeam survey aboard the R/V Tommy Munro (28–30 September); and chirp sonar and side scan surveys aboard the R/V Pelican (3–4 October) just before experiments began.

A. Preliminary Surveys

Based on logistic requirements, distribution of sediment types, environmental impact, fall meteorological and oceanographic conditions, and results from the initial reconnaissance cruise aboard the R/V Seward Johnson, the site selection process was limited to the Mississippi, Alabama, Florida (MAFLA) sand sheet, as described in [24]–[29]. Sand ridges dominate the surficial morphology of the Alabama-Northwestern Florida nearshore regions (0–20-m water depths). These sand ridges, evident in NOAA coastal bathymetry maps, are generally over 0.3 km in length, have a relief of 5 m, and are repeated every 1–4 km [29]. This type of sand ridge fits into the classification of shoreface connected ridges proposed by Dyer and Huntley [30] and is typically associated with the retreat of barrier beaches. The sediment is originally deposited as ebb tidal deltas of migrating inlets in the barrier beaches and subsequently cut off from the barrier islands [30]. The SAX99 experimental site was eventually located on a bathymetric high associated with one of these ridges (Fig. 1). Surface sediment of the MAFLA sand sheet is fine- to medium-grained (0.125–0.50 mm), moderately well-sorted quartz sand [25], [26], [31]. Carbonate content is generally less than 15%. The MAFLA sand sheet is sediment starved [32] with small-scale surface features controlled by biological reworking or bed stress from major storms or hurricanes [21], [28].

B. Site Selection

A survey of potential sites on the MAFLA sand sheet was made aboard the R/V Pelican during 8–19 July 1999, including side scan sonar (Don Walter, NRL), subbottom chirp profiling (Steve Shock, FAU), video camera drifts, grab sampling, and diver observations (Kevin Briggs, Mike Richardson, and Ricky Ray, all of NRL). A site off Fort Walton Beach, Florida ($30°22'$N; $86°38'$W) showed the greatest promise because significant near-surface acoustic scattering or layering was absent in acoustic profiles (Steve Shock, FAU). Divers found no mud lens and very little shell hash. Members of the U.S. Geological Survey, led by Nancy Dewitt, collected 10 vibra-core samples within the proposed Fort Walton Beach site during 24–29 August 1999. Acoustic observations were confirmed as a relatively thick (100–270 cm) layer of medium-to-fine, well-sorted sand was found throughout the Fort Walton Beach site. Sediments collected with the vibracores (Fig. 2) represent at least three of the sediment lithofacies previously described by McBride [29] in his analyses of vibracores collected along the Alabama–Northwest Florida coastal shelf. Lithofacies 6 is interpreted by McBride [29] to be a modern shelf sand sheet in equilibrium with recent hydrodynamic conditions. Sediments are derived from the eroding Pleistocene barrier island shoreline, transported offshore and deposited, and then extensively reworked by high-energy hydrodynamic events such as hurricanes [33]. The result is thick (1–5 m) well-sorted fine-to-coarse quartz sand with widely scattered carbonate shell fragments. Lithofacies 5 is a thin well-developed clast- or matrix-supported marine shell bed. McBride [29] suggests this facies formed at the base of the high-energy shoreface and was mixed with and then buried by the sand deposition (Lithofacies 6). Lithofacies 4, a horizontally-laminated, silty-clay (1–4 m thick) layer deposited under estuarine conditions, was evident at the bottom of some of our vibracore samples. Experimental constraints, which required (i.e., Lithofacies 6), appear to be met at this site. The distribution and range of depth of lithofacies 6 near the Fort Walton Beach site was further characterized during subsequent multibeam sonar and chirp sonar surveys.

C. Acoustic Site Characterization

An EM 3000 multibeam echosounder (Roger Flood, SUNY), mounted on the R/V Tommy Munro, was used to survey the

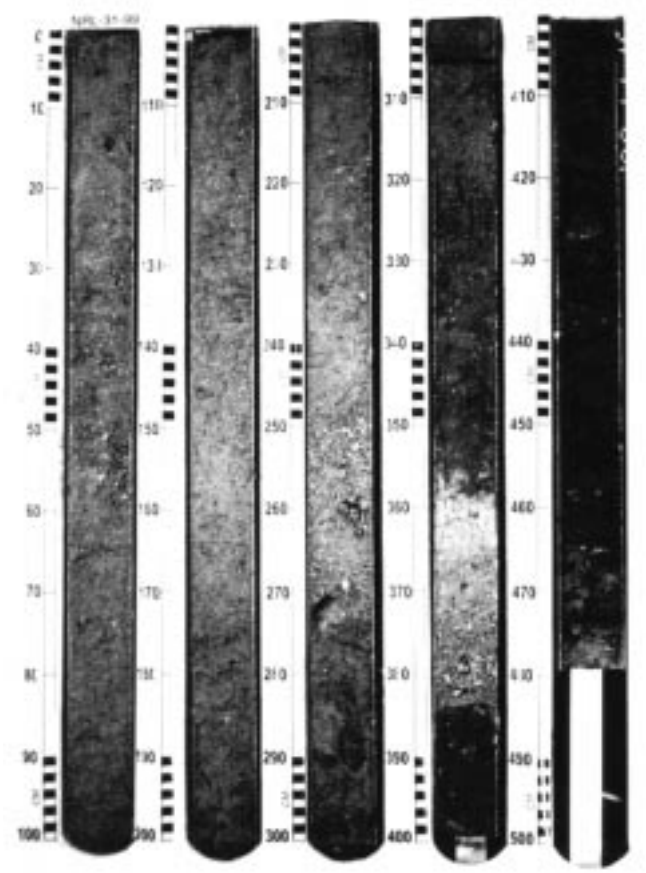

Fig. 2. Photograph of sediments collected with a vibracorer (site 31) near the center of the SAX99 experimental site. Lithofacies 6 (0–360 cm) is clean, well-sorted fine-to-medium quartz sand; lithofacies 5 (360–385 cm) contains considerable shell fragments; and lithofacies 4 (385–454 cm) is dark medium sand mixed with numerous wood fragments, mud, and layers rich in organic matter.

seafloor in the Fort Walton Beach experimental area immediately prior to the beginning of the acoustic experiments (28–30 September, 1999) [34], [35]. The EM 3000 multibeam echosounder, which operates at 300 kHz, provides high-resolution bathymetry and backscatter data to map the seafloor. Bathymetric data has a nominal vertical accuracy of about 5 cm and the backscatter data is reported as dB. Bathymetric and backscatter data have a nominal horizontal accuracy of better than 1 m. The EM 3000 generates up to 120 beams spaced 0.9 degrees apart to map a swath that is four times the water depth. Backscatter strengths are sampled at higher across-track frequency, resulting in more detail in the backscatter record than in the bathymetric record.

The objectives of the multibeam survey were to: 1) characterize the morphology of the planned study area; 2) evaluate variability of backscatter strengths; and 3) determine the dependence of backscatter strength on angle of incidence. Survey lines with a spacing of two times the water depth and girded at 1 m were first used to survey a region somewhat larger than the final study area. A tide recorder in the study area recorded sea-level variations during the survey, and CTD profiles were taken to determine sound velocity structure in the water column. The results of this survey were available immediately and show that the region studied is characterized by a series of ridges or plateaus that dip to the south and east (Fig. 3). Distinct downslope trending troughs or channels separate the ridges. Some of the troughs cross the study area trending offshore while other troughs have more limited downslope extent. One of the more prominent troughs has a depth of about three meters and a width of about 200 m. There is a distinctive smaller channel at the base of this trough. The floor of all of the troughs have backscatter strengths about 10 dB lower than the ridges. Regions of lower backscatter strengths in the troughs are characterized by fine-grained sediment while regions of higher backscatter strengths are characterized by fine-to-medium sand. The trough crossed fairly near the planned study site, and the proposed sampling sites were therefore shifted up onto the ridge where sediments are at similar depth and have similar backscatter values. Survey lines were then run close together so that the same portion of seabed was covered on a number of adjacent tracks. Lines were also run at a number of headings to evaluate the azmuthial dependence of backscatter strength. Initial detailed analysis of the backscatter strength suggests that the EM 3000 can resolve the individual bottom ripples (reported by divers to be spaced 0.5–1 m apart) in 20 m of water, especially when the swath is oriented perpendicular to the ripple crests. However, the ripples are not resolved in the bathymetric data.

A multiband chirp sonar survey (Steve Shock, FAU) was conducted at the Fort Walton Beach site on the 3rd and 4th of October 1999 to confirm that the top meter of sediment in the survey area did not have inhomogeneities that might interfere with high frequency bottom interacting acoustic experiments and to collect data to be used for sediment property prediction [36]. While being towed approximately 4 m above the seabed, the multiband chirp sonar simultaneously transmits three FM pulses over three adjacent frequency bands covering the range of 1 to 45 kHz. Normal incidence reflection profiles were measured with two planar arrays with dimensions of 0.75 by 0.75 meter and 4 by 4 cm. Reflection profiles are generated from the output signal of the 0.75×0.75 m planar array after applying a low pass filter with a cut off frequency of 8 kHz (Fig. 4). These profiles demonstrate a thickness of first layer (lithofacies 6) between 1 and 3 m over most of the study site. A second layer, characterized by higher backscattering strengths (lithofacies 5) probably represents the well-developed clast- or matrix-supported marine shell bed described by McBride [29]. Below this layer occasional horizontally laminated layers probably representing the silty-clay layer (lithofacies 4) deposited under estuarine conditions are evident. Reflection profiles of the top meter of sediment along the westernmost N-S track line were generated by removing the water column data from the output of the 4×4 cm planar array using the full operating band of 1–45 kHz. The images show that the vertical resolution of the sonar approaches 1 cm allowing the measurement of the height of sand ripples and the thickness of a thin mud layer over the sandy seabed. The images also show the size and locations of sediment inclusions within the top meter of sediment.

III. Meteorological Conditions

Meteorological conditions in the northeastern Gulf of Mexico during October and early November are generally transitional

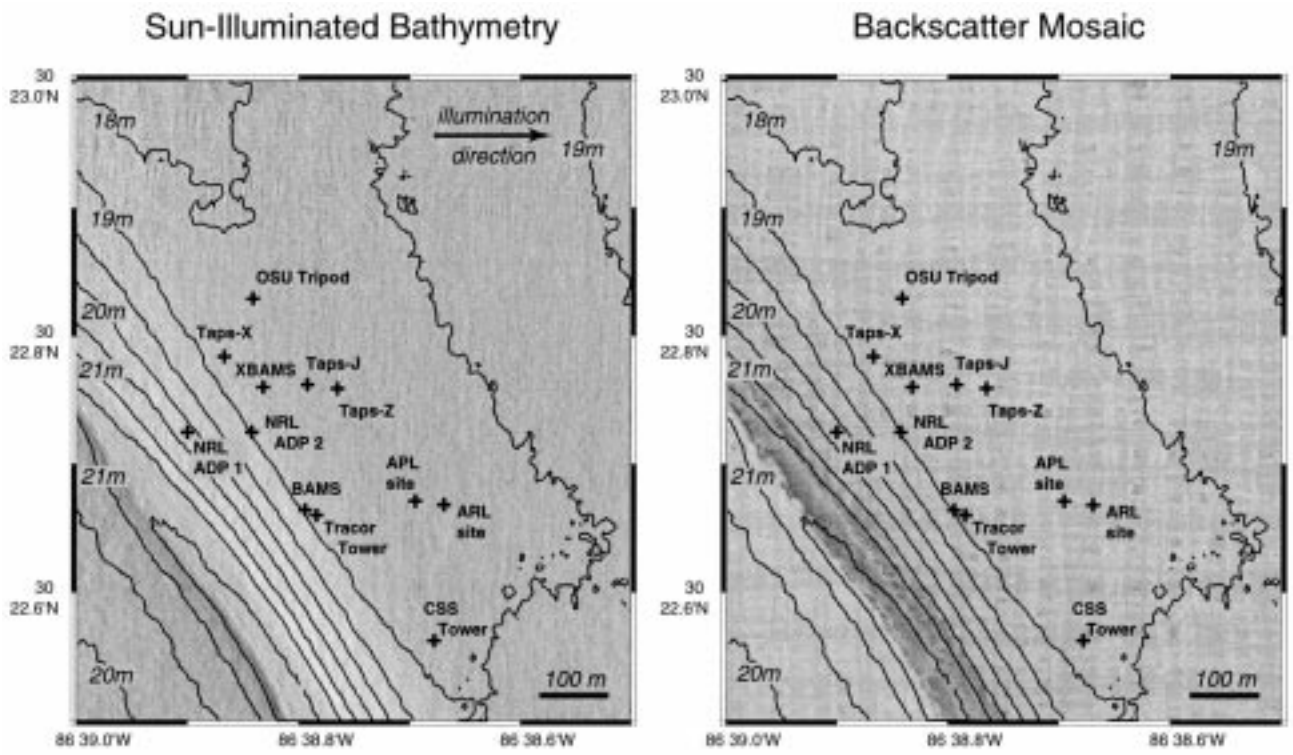

Fig. 3. Multibeam maps of the SAX99 study area. Both maps show 0.5 m bathymetric contours and bottom station locations (+). The contours show a 3 m deep, 200 m wide trough or channel trending downslope in the southwest part of the study area. The stations are located on a flat ridge to the east of the trough. Left: Bathymetric contours and station positions superimposed on sun-illuminated bathymetry. This map shows that floor of the trough contains a distinct small channel with a width of about 10–20 m and a depth of about 20 cm. Right: Bathymetric contours and station positions superimposed on a mosaic created from the EM 3000 300 kHz backscatter data. Higher backscatter is lighter, and the checkerboard pattern on the backscatter map is related to tracklines. The trough has lower backscatter than the flat area to the west (note that the region of low backscatter is offset from the trough floor, and extends slightly up the eastern channel wall). Backscatter (gridded at 1 m) appears fairly uniform near the stations.

between the relatively calm hot summers and the windy colder winter months. The Atlantic (Bermuda) High, drives a persistent southerly flow of humid air over the region between late spring and summer. During late fall through early spring, the Atlantic high retreats southward allowing polar fronts to make between 20 and 30 incursions into the area [37], [38]. Hurricanes make landfall approximately once every 7 years. We were fortunate that tropical weather systems including hurricanes Irene (13–19 October) and Jose (17–25 October) as well as tropical storms Harvey (19–22 September) and Katrina (28 October–1 November) had no major adverse impact on the experiments. Both Tropical Storm Harvey and Hurricane Irene were in the Gulf of Mexico near or during the time of the experiments but crossed land in southern Florida and remained in the Atlantic Ocean. Neither system produced strong winds or high sea states at the experimental site or at the closest NOAA NDBC data buoy (Fig. 5). Two strong cold fronts that past through the area in [22–23 October (Julian dates 295–6); 2 November (305–306)], three weaker cold fronts [29–30 September (272–273); 4–5 October (277–278) and 17–18 October (290–291)], and a low-pressure trough [9–10 October (282–283)] dominated weather conditions. Meteorological observations were measured by weather instruments on the R/V Pelican (3–28 October) and R/V Seward Johnson (14 October–10 November), and were available from the local weather station at Eglin AFB ($30°29'\mathrm{N}$; $86°32'\mathrm{W}$), and from a NDBC 3 m data discus buoy (42039) moored in 285 meters of water 104 km south of Panama City, Florida ($28°47.08'\mathrm{N}$; $86°02.27'\mathrm{W}$).

Recorded wind speeds during the experiments (1 October–10 November) were higher at the two ships ($10\,\mathrm{m{\cdot}s^{-1}}$) and the NOAA buoy ($6.8\,\mathrm{m{\cdot}s^{-1}}$) than at the Eglin AFB 2 $\mathrm{m{\cdot}s^{-1}}$). The highest wind speeds were recorded after the passage of cold fronts on 24 October (Julian date 297), 1 November (305), and 3 November (307). The passage of cold fronts was evident by increased wind speeds, a change in wind direction, and changes in barometric pressure (Fig. 5). Wind measured at the experimental sites, aboard the ships, have a diurnal component (sea breezes) not present at the inland (Eglin AFB) and offshore (NOAA Buoy) sites.

Mean air temperatures decreased from near 25 °C at the beginning of October to near 15 °C in mid-November (Fig. 6). The three sharp dips in mean air temperature were due to the passage of cold fronts on 19 October (292), 24 October (297), and 3 November (307). As will be shown in the next sections, meteorological conditions, especially associated with the passage of cold fronts, strongly affect both oceanographic conditions and seafloor characteristics.

IV. Oceanographic Conditions

A. Historical Conditions and Models

The northeastern Gulf of Mexico is characterized as microtidal with an average tidal range of 0.4 to 0.5 m. Tidal

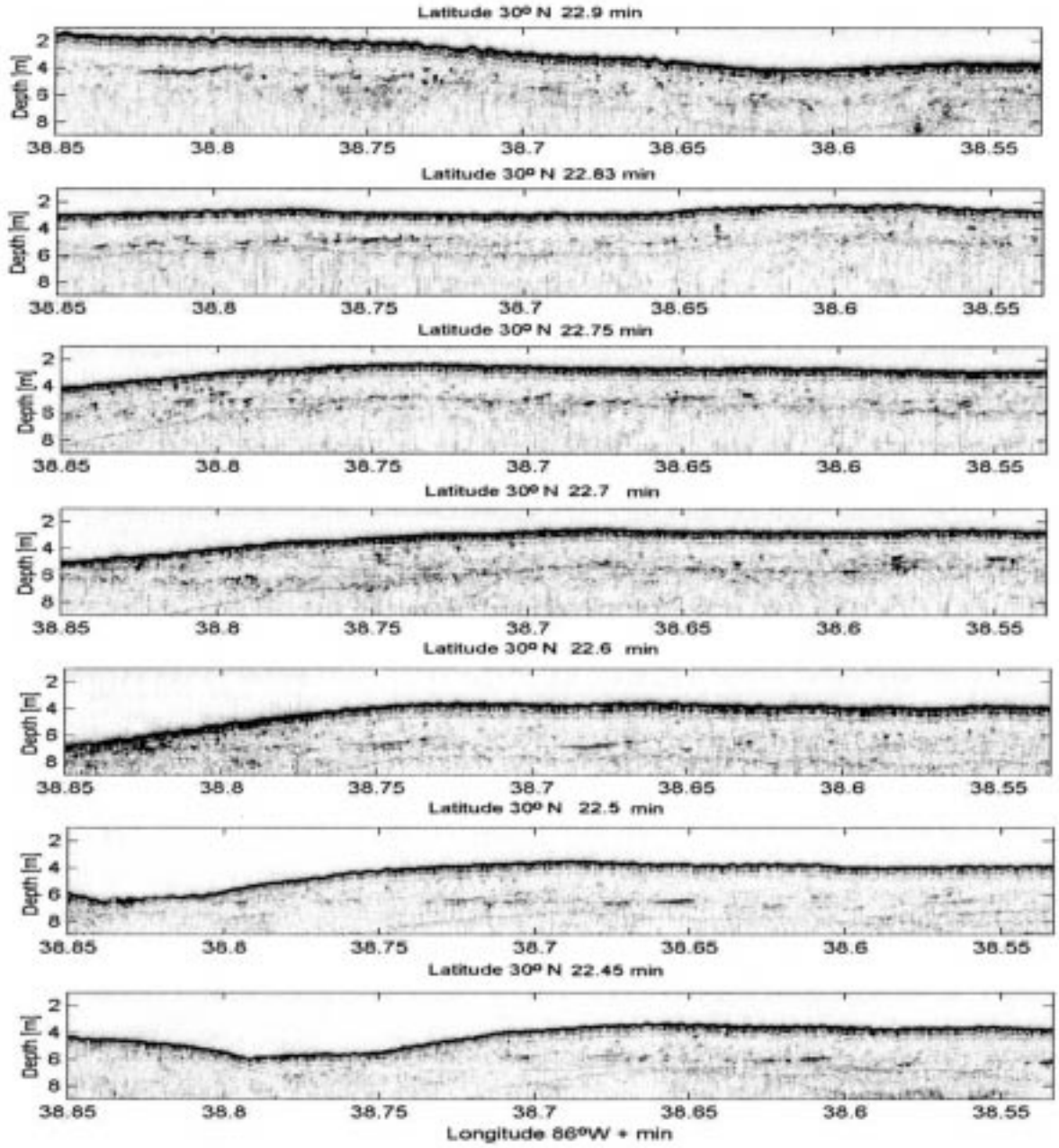

Fig. 4. Chirp sonar reflection profiles along N–S tracklines at Fort Walton Beach site collected using the frequency band of 1 to 10 kHz.

currents on the shelf are generally less than 15 cm·s^{-1} [37], [38] whereas wind driven alongshore currents can be as high as 40–50 cm·s^{-1} with strongest currents in the winter and early spring associated with the passage of cold fronts [39], [40]. Tropical storms (hurricanes) can generate currents well in excess of 100 cm·s^{-1} and rework sediments to water depths of 100 m [41], [42]. Oceanographic conditions during the October, early November time period are generally transitional between a stable, stratified water column characteristic of the summer months and the destratified water column characteristic of winter months where temperature, salinity and density increase offshore rather than with water depth [38]–[40]. During the fall period, water temperature begins to fall from highs of near 30 °C in the summer months to 15 °C in the winter. Sea state (period, direction and significant height) during the time period can be a function of both local meteorological conditions (wind speed and direction) and major tropical disturbances in the Gulf of Mexico. The passage of cold fronts appears to have a major impact on oceanographic conditions within the northern Gulf of Mexico [40], [41].

The following conceptual model for the interaction of meteorological and oceanographic conditions in the northern Gulf of Mexico provides a framework to interpret meteorological and oceanographic data collected during the SAX99 experiments. The passage of a cold front has three phases: the prefrontal phase, the frontal passage event, and the cold air outbreak/high pressure phase [40]. During the prefrontal phase the barometer falls, southerly winds strengthen leading to an onshore advec-

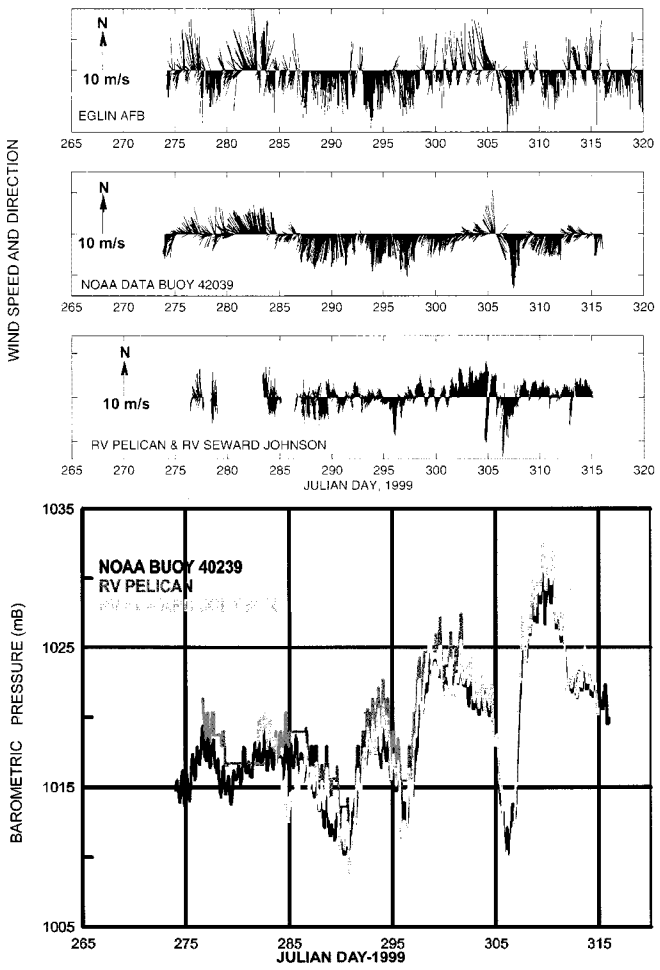

Fig. 5. Wind speeds and directions and barometric pressure measured during the SAX99 experiments at the research vessels, Eglin AFB and NOAA data buoy. All times are based on UTC and Julian dates.

tion of warm moist air, and air temperatures exhibit very small diurnal fluctuations because of the suppressed radiative and latent heat exchange. Fully developed, longer-period seas develop because strong southerly winds, long fetch, and lowering barometric pressures and the average water depth increases. After passage of the cold front, air temperature drops, winds rotate clockwise to northerly direction, skies clear, barometric pressure rises, and sea level drops. These conditions lead to increased heat fluxes from the warmer sea to the cold atmosphere and increased diurnal periodicity in air temperature and surface winds (land breeze/sea breezes). Evaporation and sensible and radiative heat losses cool surface seawater, which tends to increase surface water density. Coupled with wind stress these processes initiate turbulence and convective mixing that dissipates stratification [40]. The result is a destratification of coastal waters and the creation of cross-shelf gradients in temperature and salinity. This conceptual model is in concordance with meteorological and oceanographic observations made during of the passage of a cold front (December 1978) by Huh et al., [40] at Stage I on the continental shelf off Panama City Florida, about 85 km to the southwest of the SAX99 experimental site. A cooling rate of 0.5 °C/day^{-1} was measured in the 32-m depth destratified water column after the passage of a strong cold front (9–13 December 1978). Models based on heat balance gave a 0.4°C/day^{-1} heat loss that was in close agreement with measured rates. Models and data show evaporation, sensible heat loss and radiative heat loss accounting for 58%, 25%, and 17%, respectively, of the heat fluxes to the atmosphere. The cold fronts also reversed shelf surface and bottom water currents from the dominant slow northwestward flow to a short-lived faster southeastward flow that exceeded the threshold of sediment motion. This change in direction of flow is apparently a geostrophic response to a lowering sea level.

B. Measurements Techniques and Data Collected During SAX99

The local sea state was measured using a 0.9-m-diameter TRIAXYS™ directional wave buoy (Peter Dahl, APL) and from pressure fluctuations (4 Hz) measured at 18–19-m water depth with a bottom mounted Parascientific digiquartz pressure transducer (Richardson, NRL). The directional wave buoy measured spectral variance in 0.005 Hz frequency bins from 0.060 Hz to 0.64 Hz, and in 3° directional bins from 0° to 357° (note that significant wave height, or $H_{1/3}$, is computed here using $H_{1/3} = 4\,(H^2)^{0.5}$ where H^2 is the mean square wave height). Additional data on regional sea state conditions were available from NDBC buoy 42 039. Depth profiles of temperature, conductivity, oxygen concentration, optical fluorescence, transmission, and irradiance were measured three times a day using a Seabird 911 plus CTD (70 profiles) aboard the R/V Seward Johnson. From these data salinity, density and sound speed were calculated. One CTD profile was also collected aboard the R/V Pelican. Additional data on bottom water temperature and conductivity (yielding calculated salinity and sound speed) were measured every 15 minutes using a bottom-mounted Seabird MicroCat from 3 October through 10 November 1999 (Richardson, NRL). Surface temperature and salinity were also measured every 5 minutes using the flow-through seawater pumping system of the R/V Pelican and R/V Seward Johnson. Near bottom currents were measured every 15 min with a bottom-mounted Sontek ADCP. Hull-mounted RDI BB600 ADCP's were used to measure current speed and direction from both the R/V Seward Johnson and R/V Pelican but have not yet been analyzed.

Changes in meteorological and oceanographic observations appear to be primarily related to the passage of cold fronts during the experiment. The conceptual model described by Huh *et al.* [40] appears to account for changes in meteorological and oceanographic conditions during the passage of cold fronts during the SAX99 experiments (Julian dates 292–293, and 307) (see Figs. 5–8). Surface and bottom waters are well mixed as indicated by similar surface and bottom water temperatures (Fig. 6). Rates of surface and bottom water cooling (0.5°C day^{-1}) measured between Julian dates 290–298 are in general agreement with the model predictions and observations made by Huh *et al.* [40], but the 0.8°C/day^{-1} decrease in surface and bottom water temperature between Julian dates 307–311 is greater. Two cold fronts contributed to the air and water-cooling during Julian dates 290–298 and a single strong cold front (Julian date 307) resulted in air and water cooling between Julian dates 307–311. Near bottom currents were

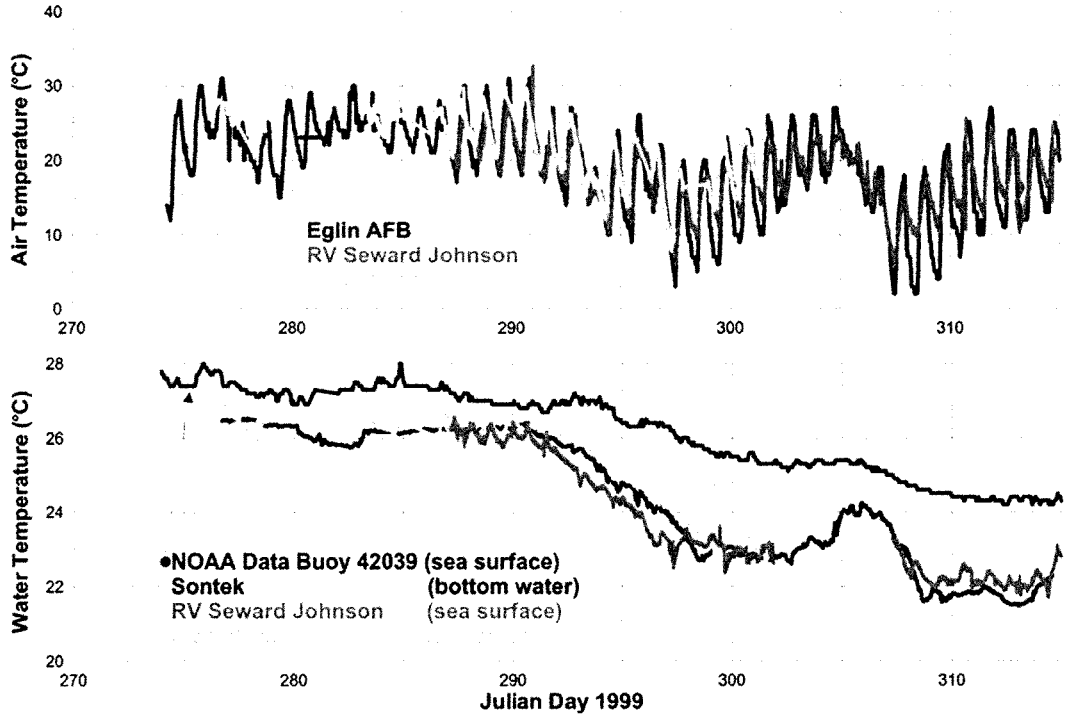

Fig. 6. Air temperatures measured at Eglin AFB and the two research vessels; surface water temperatures measured by the NOAA data buoy and the R/V Seward Johnson; and bottom water temperature measured using a SeaCat bottom mounted conductivity system. All time are based on UTC and Julian dates.

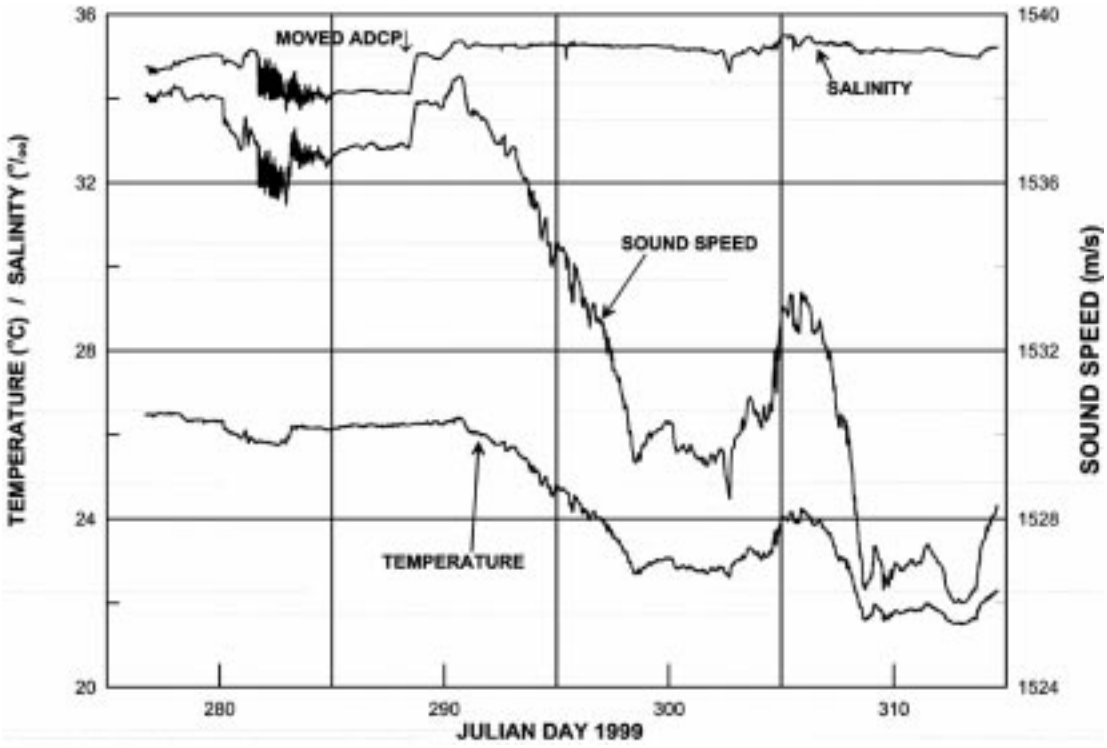

Fig. 7. Bottom temperature, salinity, and sound speed measured with a Seabird MicroCat during the SAX99 experiments. All times are based on UTC and Julian dates.

faster just after the passage of the aforementioned cold fronts than the typical 10–15 cm·s^{-1} tidal currents (Fig. 8). The direction of bottom currents generally rotates with changes in tidal flow during low flow conditions but during stronger current flows (Julian dates 290–293, 296–298, and 307–308) the current flow direction is toward the SE $(115°)$. These data again agree with the observations and models of Huh *et al.* [40]. A flow toward the SW $(245°)$ was measured between Julian dates 282–284 and was associated with a low-pressure trough and strong associated winds from the southwest. These

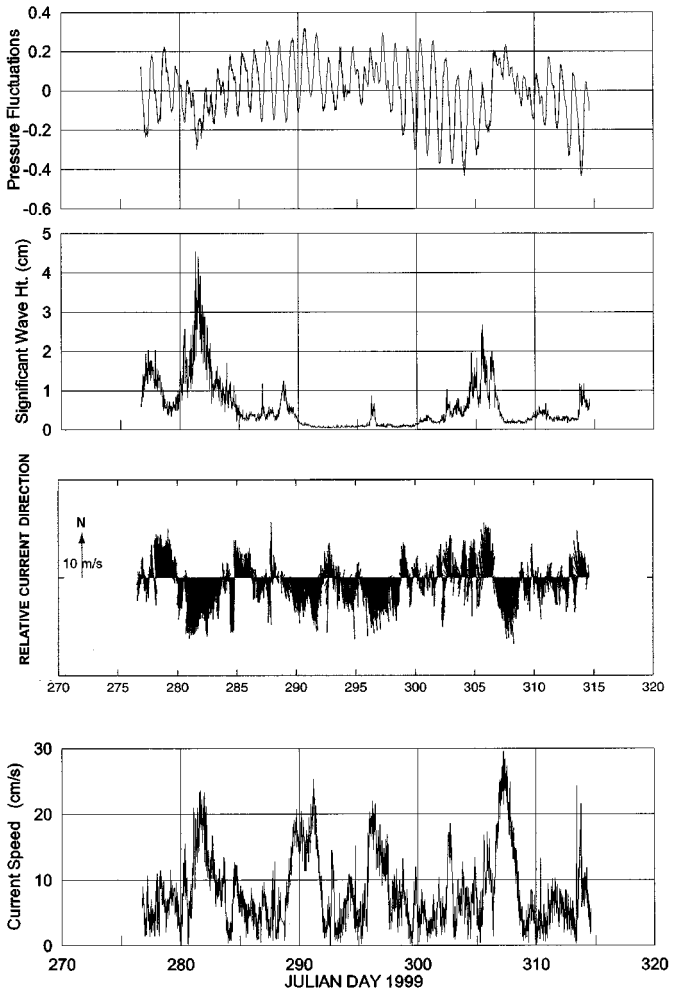

Fig. 8. Bottom current speed and direction measured at 2-m height above the seafloor with a bottom-mounted Sontek ADCP; bottom pressure fluctuations and calculated wave heights measured with data collected with a pressure transducer. Times are UTC and Julian dates.

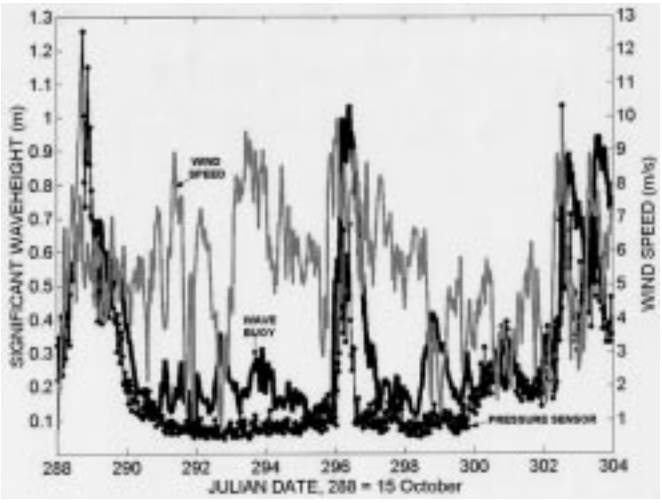

Fig. 9. Time series of significant wave height and wind speed versus Julian Day. Black line is data from APL-UW wave buoy; dashed line is data from NRL-SSC bottom-mounted pressure sensor; gray line is wind speed as measured from the Seward Johnson at a height of 19 m. All times are UTC. Larger events in the time series of significant wave height tend to lag corresponding events in the time series of wind speed by about 3–6 h.

strong southwest winds were responsible for the highest sea states (2–4 m significant wave heights) during the SAX99 experiments (Fig. 8).

Significant wave height calculated from bottom pressure fluctuations and measured with the directional wave buoy were in general agreement over Julian dates 288 through 304 (Fig. 9), a period of relatively calm sea conditions. The buoy was moored with a compliant mooring system, approximately 100 m west of the Seward Johnson's moored position, and the wave data were telemetered back to the Seward Johnson continually every $1/2$ hour starting from UTC 1430, 13 October and ending at 2130, 11 November. The exception to this is UTC 2230, Oct 14 to 2130 Oct 15, during which the buoy was shut down. Winds of sustained duration most frequently originated from an east to southwest direction $(90\text{–}180°)$ and produced a peak in the directional wave spectrum within the same directional range (wave direction is defined by the buoy's directional processing algorithm as direction from which the waves are propagating). This is exemplified by Fig. 10 that shows a directional wave spectrum during which the wind speed was 7–8 $\text{m}\cdot\text{s}^{-1}$ over several hours. The directional wave data collected with the TRIAXYS™ directional wave buoy will be used to construct 2-D surface wave correlation functions, from which the sea surface bistatic scattering cross section will be computed [43]. The scattering model results will be used to interpret data originating from the synthetic aperture sonar (SAS) trial conducted at the SAX99 site on 28 October by the Coastal Systems Station [1]. Additional sea surface scattering measurements collected by APL-UW over the duration of SAX99 will also be analyzed together with the wave buoy data. Finally, the time series of significant wave height and mean direction obtained from the wave buoy and the Parascientific pressure sensor can be used to help interpret changes in bottom morphology as influenced by shallow water gravity waves.

C. Effects of Meteorological and Oceanographic Conditions on Seafloor Stability, Microtopography, and Pore Water Properties

The effects of surface gravity waves and bottom currents on sediment mobility and subsequent bedform morphology are based on measurements of tidal and storm-induced bottom currents, calculated orbital motion from surface gravity waves, (Figs. 8 and 9) and seafloor properties (see Section VI). Preliminary estimates of the threshold of motion and resultant changes in bedform morphology were made using the program SandCalc, a program developed by HR Wallingford Inc to accompany the text by Soulsby [44]. The threshold velocity for fine sand particles (0.25–0.50 mm) at 2 m above the seafloor ranges from 0.47 to 0.50 $\text{m}\cdot\text{s}^{-1}$, which was not exceeded at any time during the SAX99 experiments (Fig. 8). This suggests that tidal or storm-induced bottom currents, which had a maximum speed of 30 $\text{m}\cdot\text{s}^{-1}$ at 2 m from the seafloor, were not sufficient to move sand particles or change sediment morphology. By contrast, the threshold orbital velocity for motion of sediment by waves is exceeded for wave heights greater than 1.0 m, which occurred at least twice during the SAX99 experiments

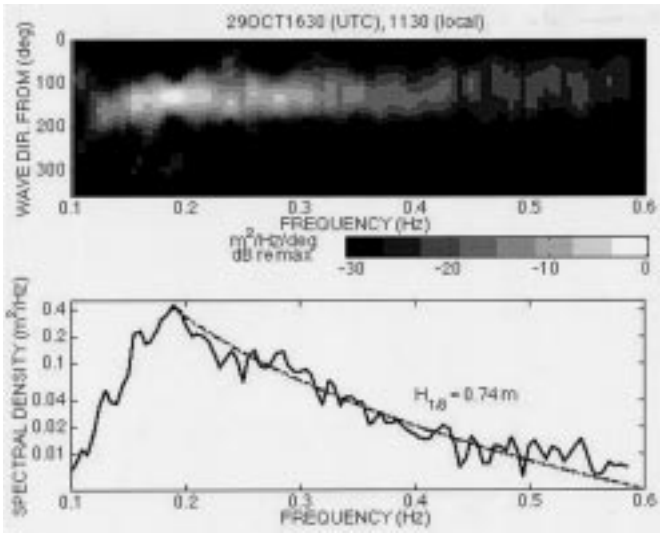

Fig. 10. Two-dimensional directional wave spectrum as measured by the wave buoy, showing wind-generated waves oriented in the same direction as the wind, which originated from an south-east direction with an average speed of 7–8 $\mathrm{m \cdot s^{-1}}$. The upper plot is the distribution of wave energy with frequency and direction. The light-to-dark range in intensity indicates a high-to-low spectral density range of three orders of magnitude. Lower plot is the frequency spectrum and the dashed line shows a F^{-4} spectral decay with frequency.

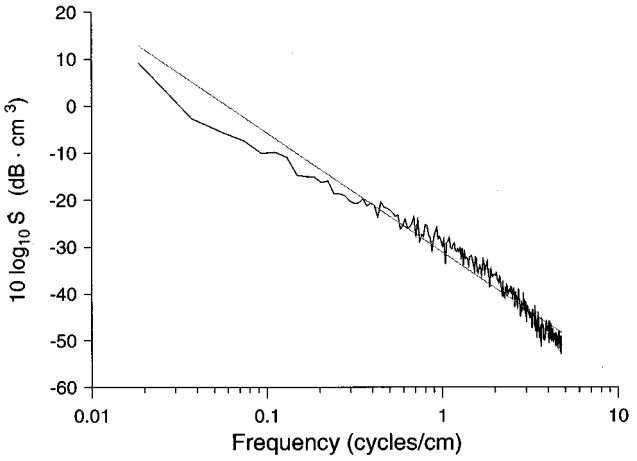

Fig. 11. One-dimensional roughness power spectrum estimated from analog stereo photographs. Slope of the spectrum is —2.54 and the intercept (at 1 $\mathrm{cm^{-1}}$) is 7.71×10^{-4} $\mathrm{cm^3}$.

(Fig. 8). Sand ripple wave heights ranging between 7–10 cm and wavelengths between 50–70 cm are predicted for significant wave heights between 2 and 4 m. These predictions are in agreement with diver observations and photographic evidence. More detailed calculation bed stresses and resultant bedform modification will made when all the data are analyzed, including the water column currents from the ship mounted ADCP.

V. Seafloor Roughness

Several methodologies (photographic and laser line scan technology, analog and digital recording methods, and emulsion and magnetic tape media) were employed to measure seafloor roughness to help understand the contribution roughness at the sediment–water interface to acoustic scattering [11]. Three efforts involved a mobile apparatus capable of gathering roughness information at different locations, whereas the other two efforts documented temporal changes in bedforms at their deployment locations.

A. Analog Stereo Photographs

A Photosea 2000M diver-operated stereo camera with 150 J strobe (Kevin Briggs, NRL) was used for close-range (91 cm) photogrammetry to determine seafloor roughness at several locations within the experimental area (Low-Frequency, APL Tower, BAMS, and APL Penetration sites). The stereo camera and strobe were mounted on a PVC stand and were deployed on the sea floor using a fiberglass measurement tape to provide scale and direction to the photographs [45]. A set of carpenter's levels was used at the acoustic penetration site to provide orientation information on small-scale (3.6-m) seafloor slope.

The film was developed as continuous rolls and then sectioned into stereo pairs for later manual photogrammetric analysis with a Benima stereo comparator. Selected stereo pairs were digitized over a 55×72 cm overlap area to acquire three independent 54-cm-long cross-sectional transects digitized for calculation of one-dimensional roughness power spectra. A roughness spectrum representing an average of twelve 54-cm-long transects was estimated for the stable seafloor roughness present from 23 October to 5 November (Fig. 11). The slope of the spectrum (-2.54) is relatively steep as a result of very little high-frequency roughness. This lack of high-frequency height fluctuations is typical of smoothed, decaying ripples. There is considerable variation in the spectrum, based on deviations from the regression line. The deviations from the regression indicate that the spectrum slope and strength should be determined from spatial frequencies pertinent to the acoustic wavelength of interest.

B. Time-Lapse Stereo Photography

Rob Wheatcroft, Oregon State University, deployed a tripod consisting of a Photosea 2000 stereocamera and a Sontek Hydra system (acoustic doppler velocimeter, pressure sensor, turbidity sensor, and conductivity/temperature sensor) at a site northwest of the main experiments (Fig. 3) for 34 days. Equipment problems limited the available data set to 15 days of stereophotographs and 1 day of oceanographic data for the Sontek system. The stereophotographs cover a 2×1 m section of the seafloor and were taken every 6 h.

C. Digital Stereo Photographs

A digital close-range photogrammetry system using charge-coupled device (CCD) cameras was also used to create stereo images of the sea floor (Tony Lyons, SACLANT Undersea Research Centre). Digital cameras and photogrammetric processing software produce surface elevation models in the form of a digital elevation model (DEM). From secondary analysis performed on the DEM's, relative sediment height and two-dimensional roughness spectra are estimated. The full photogrammetry system consists of a frame, waterproof housings, serial communication cables, digital cameras, strobe, and a personal computer to run the acquisition, image enhancement, registration, and stereo-correlation software.

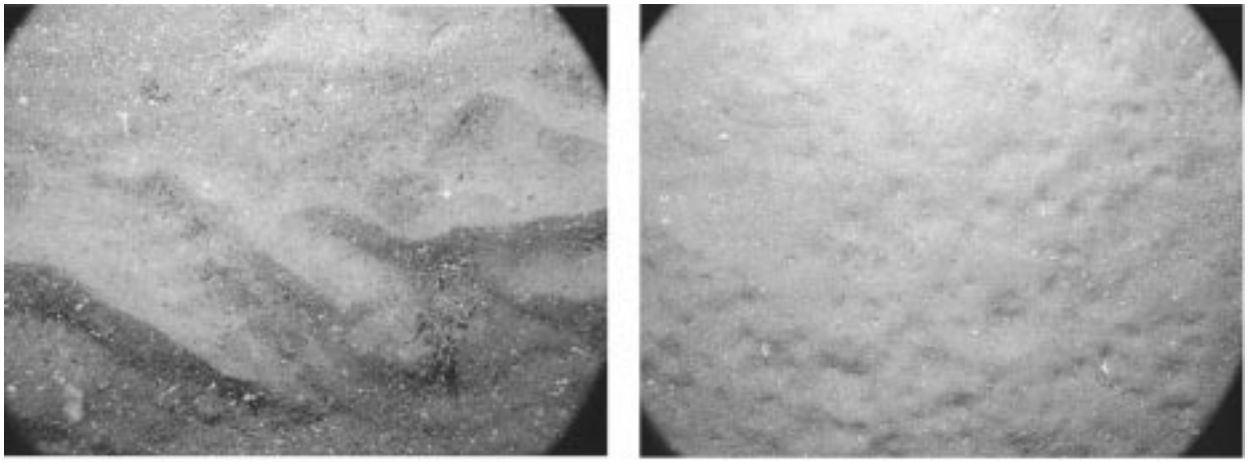

(a) (b)

Fig. 12. Bottom photographs taken with the SACLANTCEN digital stereo camera: (a) sharp-crested, well-defined ripples present at the beginning of the experiment and (b) small pockmarks created by feeding fish.

Kodak DC120 digital cameras with a resolution of 1280×960 pixels are used in the image acquisition system. The CCD sensor is advantageous for photogrammetric applications as it gives improved sensitivity, has area utilization rates approaching 100% and does not require fiducial marks because the regular array of light sensitive elements within the CCD image sensor are used as a photo-coordinate system. The two digital cameras are mounted on a frame in watertight containers that are connected by a serial cable to a shipboard computer for real-time acquisition of digital images. A 100-J strobe is attached to the frame for use as a light source in low-light conditions. The cameras are oriented with their axes angled 4° inwards and provide a convergent geometry at the 91 cm distance sea floor, which allows a base-to-height ratio of 0.35.

The Desktop Mapping System (R-Wel Inc.) performs stereo-correlation calculations of the digital images using a stereo-correlation algorithm that makes use of area-based matching. Area-based matching, a simple technique for finding corresponding points on two registered stereo images, searches a sub-window in the two images by comparing an even smaller sub-window until the correlation is maximized. The final product is the full 2-D height field from which the full 2-D roughness power spectrum can be estimated. Before being Fourier-transformed to the frequency domain, data segments are multiplied by a tapering function. A zeroth-order discrete prolate spheroidal sequences data taper is used on the rectified and stereo-correlated data sets for optimizing bias/resolution trade-off [46]. This kind of technique yields rms errors on the order of a pixel [47]. The effective horizontal and vertical resolution of this system is approximately a millimeter.

Digital (and duplicate analog) images were first collected at the Low Frequency and Benthic Acoustic Measuring System (BAMS) tower sites. At the beginning of the experiments, seafloor roughness was characterized by well defined, sharp-crested ripples [Fig. 12(a)], but over the duration of the experiment the ripple field was altered by hydrodynamic and biological processes, resulting in a more subtle and complex morphology. Finally, digital images were collected as a time-series at the anchorage site from the R/V Seward Johnson, where alteration of the sea floor by the activities of fish was intense [Fig. 12(b)].

D. Laser Line Scanner

A laser line scanner, using the technique of structured lighting, was used to measure seafloor topography (Jules Jaffe, Scripps Institution of Oceanography). Structured lighting permits both longer range and higher resolution imaging because the volume of backscattered light between source and receiver is reduced. In addition, structured lighting provides unambiguous correspondence between source and receiver characteristics, a necessary condition for any procedure that utilizes triangulation methods for range measurement [48].

The system, *3D Sea Scan*, consists of a high-power (3-W) pulsed laser at a wavelength of 532 nm, a fast 1-D CCD camera, scanning mirrors, and ancillary electronics. The system acquires line-by-line data by scanning the sea floor athwart ships with the CCD camera concurrently viewing the same plane of illumination. Light reflected back into the camera consists of volume scattering within the plane as well as reflected light from the sea floor. If the water is sufficiently clear and there is adequate bottom reflectance, individual positions on the sea floor can be imaged. With knowledge of system geometry, both the reflectance of the bottom and the range of the position from the system can be computed. During these experiments, the *3D Sea Scan* was attached to the underside of a rail system, supported 2.8 m above the sea floor by a scaffolding, and was moved at a constant velocity across the seafloor. This approach provides repeatable and accurate bathymetric information over the two-dimensional field of view. The rail system was secured to the sea floor with several screw anchors to minimize frame rocking in currents. A thin (1-mm-diameter) white rope was suspended 1.2 m above the sea floor from one corner of the frame to another corner. Position along the track is deduced from the position of the rope in the image, measured using a 30 cm ruler in the daytime and provides unambiguous information about system position whenever data were acquired. During the intense data gathering part of the experiment, a series of measurements at the

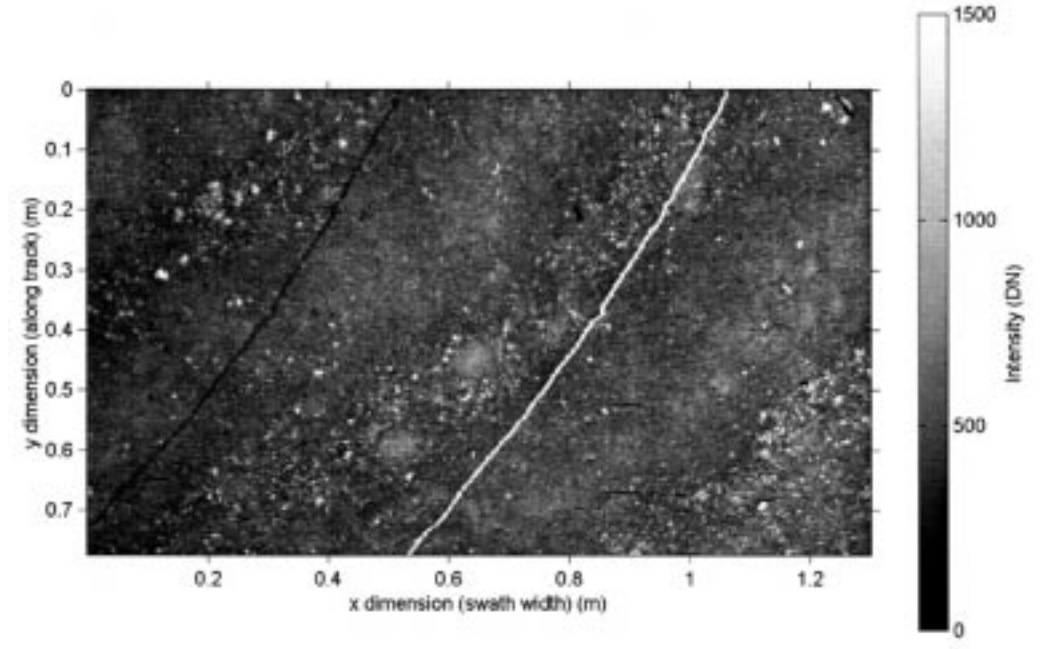

(a)

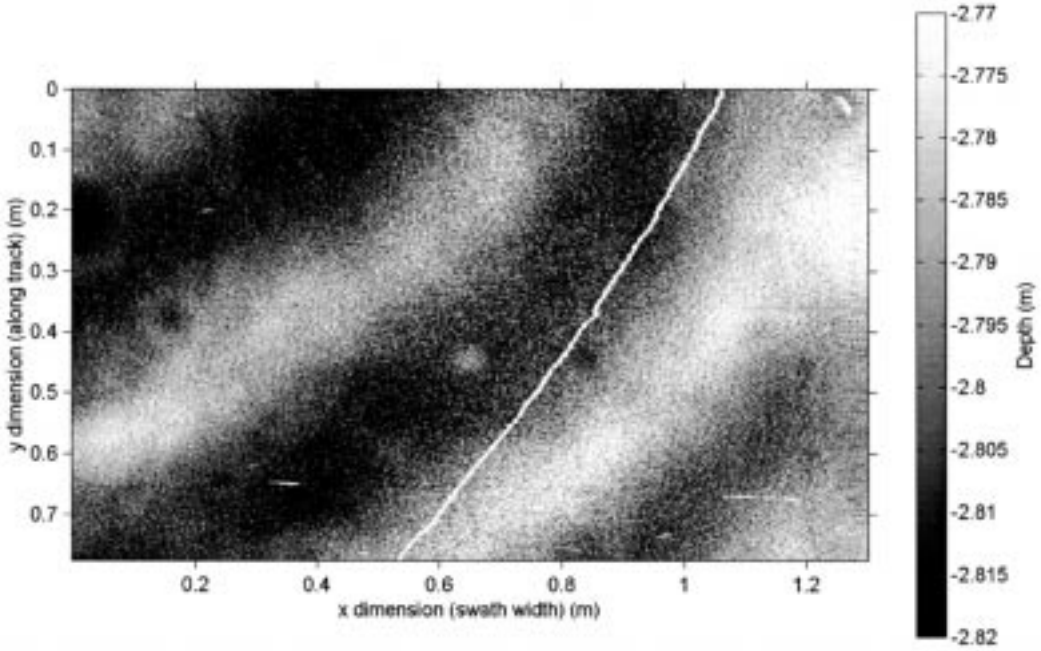

(b)

Fig. 13. A set of 2-D images of (a) reflectance and (b) range obtained by the *3D Sea Scan* laser line scanner. Approximate dimensions and number of sampled points are (horizontal 1.3 m, 512; vertical 0.84 m, 700).

same position (a 1.29-m bottom swath imaged at a range of 2.8 m) was used to examine the effect of averaging. The results indicate that the system's bathymetric resolution for a single profile is in the range of 2–3 mm. Averaging 512–1024 of these profiles resulted in a standard deviation that was close to 0.3 mm.

Four sand wave crests and three troughs with amplitudes of 2–3 cm and a periodicity of ~ 0.7 m are evident in images acquired with the system (Fig. 13). The more uniform reflectance regions (possibly representing smaller sized sand grains) tend toward the crests, whereas the more speckled regions (possibly representing larger grains and shell particles) tend to the troughs. Small crater-like formations evident in the left portion of the range image are not apparent in the reflectance image. These crater formations appear to be more numerous in the troughs and the lower sides of the sand crests, and are likely a result of animal activity.

E. Laser

A simple method of measuring sediment surface roughness, integrated with the University of Texas-Applied Research Laboratories (APL) acoustic data acquisition system (Nick Chotiros),

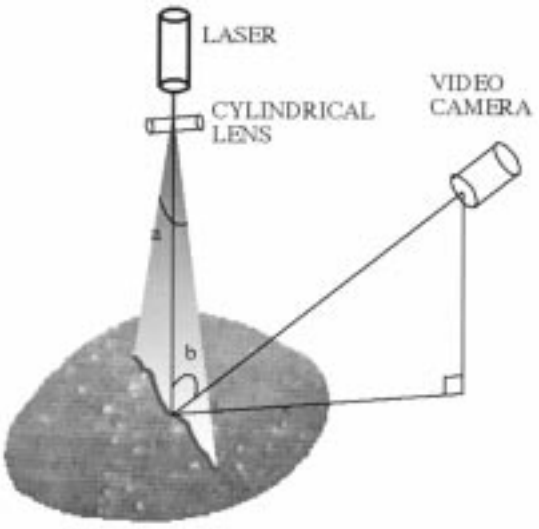

Fig. 14. Measurement of bottom roughness using a laser stripe technique.

allowed roughness measurements to be made over the ARL experiment site without interference with the acoustic data acquisition process. The method employed lasers mounted on the remotely operated vehicle (ROV). Each laser was a red He-Ne class IIIa with output power less than 5 mW. At this power level, no special precautions were needed in handling the laser other than avoiding direct eye contact. A cylindrical lens was used to spread the laser beam into a fan, which was directed downward to produce a stripe on the sediment interface. Viewing from an oblique angle, one obtains the profile of the sediment directly under the stripe (Fig. 14). The fan beam angle, α, is not very critical. It simply has to be small compared to the maximum slope on the sediment surface to avoid shadowing problems; slopes typically do not exceed $10°$. It has to be large enough to illuminate a stripe on the sediment surface of sufficient length to cover the features of interest. A 1-m stripe would be desirable, but in practice, due to a tapering of the laser beam intensity, a usable stripe length of about half a meter was obtained. The video camera sees the profile of the sediment under the laser stripe reduced in the vertical direction by the sine of the viewing angle, b. Ideally, the angle b should be $90°$ for maximum sensitivity, but a value of approximately $45°$ was more practical.

In the experiment, two lasers were used to provide redundancy and crosscheck capability. Sediment profiles were obtained at night both with and without lights from the ROV. It is evident that the laser stripes show a large sand ripple in the sediment that is not detectable in the video imagery and with proper calibration the height of the ripple may be measured from the video image. A large quantity of video imagery of this type was recorded at various times throughout the experiment. It was observed that the bottom was rippled at the start of the experiment in mid-October, but pockmarks replaced the ripples by early November.

VI. Seafloor Physical and Geoacoustic Properties (Laboratory)

Sediment properties were investigated through collection of pore water, using syringes, or sediment, using diver-collected cores, and subsequent analysis aboard ship or at ashore laboratories. Core samplers were inserted in the sediment with careful attention assigned to orientation (normal to the sea floor), constant insertion pressure, and minimal disturbance during penetration into the sediment. In this way, relatively undisturbed samples were collected for obtaining reliable measurements of sediment porosity, bulk density, grain density, grain size distribution, sound speed, sound attenuation, total organic carbon, total calcium carbonate, and gas content. Collection of porewater by divers was essential for validating assumptions about the physical properties of the porewater used to calculate acoustic propagation within saturated sediments.

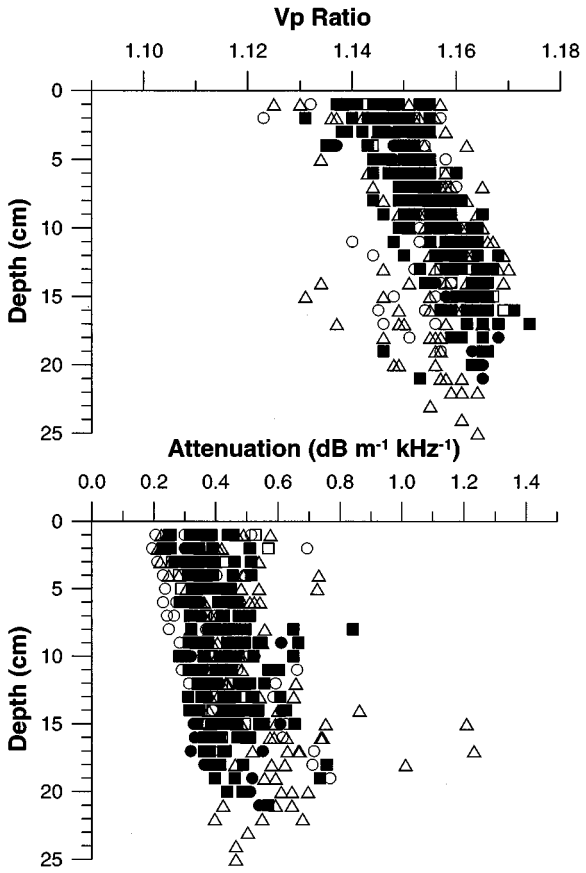

Fig. 15. Sediment sound speed ratio and attenuation measured at the following locations: Low frequency site = ○; Lopez site = •; BAMS site= □; APL site (Seward Johnson) = ■; APL STMS site = △.

A. Diver Cores

Geoacoustic Properties: Divers from the Naval Research Laboratory (Briggs, NRL) collected 27 cores (6.1 cm in diameter) from throughout the experiment area to characterize the geoacoustic variability on a fine scale (cm) vertically and on a large scale (m) horizontally. These cores were allowed to equilibrate with ship laboratory temperature for 24 h before sediment sound speed and attenuation were measured at 1 cm intervals directly through the core liner at 400 kHz [49].

Sediment sound speed (expressed as the sound speed ratio, which is the ratio of the sediment sound speed to the bottom water sound speed) increases slightly with depth in the sediment and has a coefficient of variation of 0.7% (Fig. 15). The

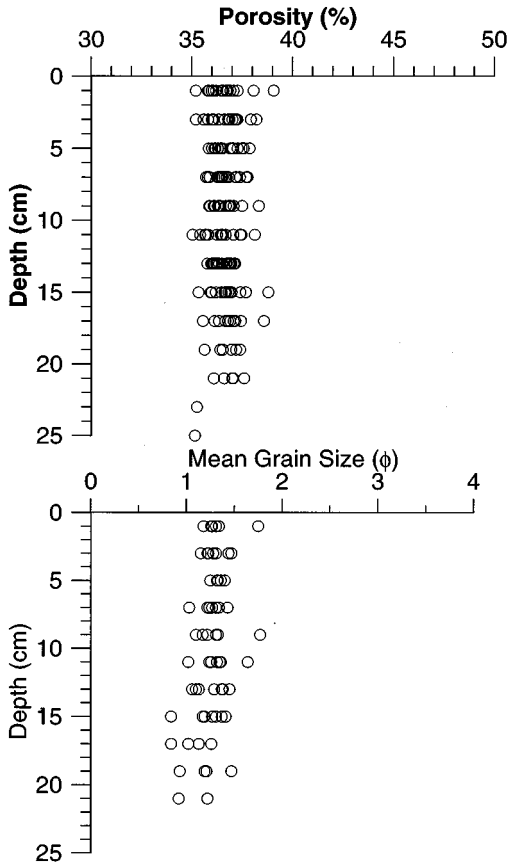

Fig. 16. Profiles of sediment porosity and mean grain size. Phi (ϕ) size is defined as the negative base 2 logarithm of the grain size in millimeters.

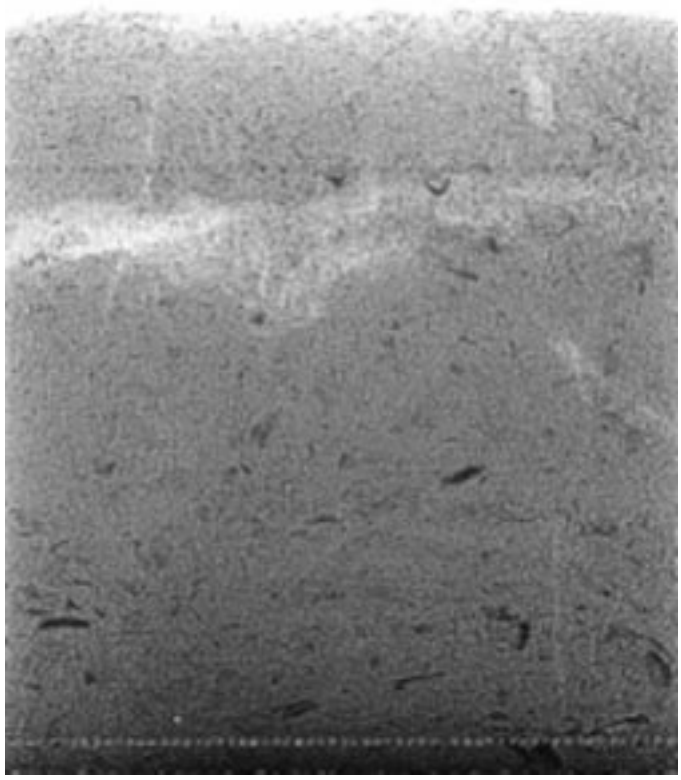

Fig. 17. Processed digital X-radiograph positive collected at the SE buoy site on 19 October. Image dimensions are roughly 12 cm wide by 16 cm deep. Processing consisted of a 3×3-sharpening mask, followed by histogram equalization. Scattered dark areas in the image are shell debris, whereas the vertically oriented light areas are animal burrows. The large horizontal light area is a mud inclusion.

variation in attenuation of the 400-kHz sound, expressed as k, or dB·m^{-1}·kHz^{-1}, is much greater than the variation in sound speed and has a coefficient of variation of 30%. This high variability may be related to scattering from shell fragments. Values and variability of seafloor geoacoustic properties are typical for sandy sediments (see [50]).

Bulk Properties: Following acoustic measurements of the NRL cores, 21 of the 27 cores were sectioned at 2-cm intervals for determination of sediment porosity, bulk density, grain density, and grain size distribution. Sediment water content was determined by water loss after sectioned samples were dried in a oven at 105°C for 24 h [49]. Porosity and density were calculated from values of water content and values of grain density measured with a Quantachrome Ultrapycnometer. The size distribution of sand-sized particles was determined by wet-sieving and pipette analysis was used to determine the silt and clay fraction. Mean grain size $(\text{mean} = 1.27\,\text{phi})$ increased slightly with depth whereas porosity $(\text{mean} = 36.6\%)$ and bulk density $(\text{mean} = 2074\,\text{kg}\cdot\,\text{m}^{-3})$ varied little with depth (Fig. 16).

Smaller 13 cm-long diver cores were collected by NRL divers at seven locations within the experimental area for sediment permeability determination. Each of 16 cores was carefully collected full, intact and sealed at the sea floor before being brought aboard ship for measurement. The cores, in their entirety, were inserted into a modified Soil Test constant head permeameter in order to approximate *in situ* measurement of percolation through the intact sediment. Five separate determinations of constant-head flow rate were made on each core. Values of hydraulic conductivity varied from 1.8 to 5.1×10^{-2} cm $\cdot$ s^{-1} (approximately 1.8 to 5.1×10^{-11} m^2 in units of intrinsic permeability).

A total of 54 digital X-radiographs were obtained by Oregon State University (Rob Wheatcroft) from 8 sites within the study area. Each X-radiograph imaged roughly 15 cm by 25 cm $(W \times H)$ of the sediment column at a 0.125 mm spatial resolution and a 12-bit gray-scale resolution. Preliminary analysis of the X-radiographs indicates the primary volume inhomogeneity to be shell debris, with a secondary contribution from animal burrows and scattered mud inclusions (Fig. 17). There is little indication of between-site differences within the study area.

Dick Bennett (SEAPROBE Inc.) measured total organic carbon (TOC) and total calcium carbonate on 25 diver-core subsamples provided by Rob Wheatcroft. Total organic content is low as expected for sandy sediments with values ranging between 0.30 and 0.77%. Total $CaCO_3$ ranged between 2.0%–5.1% and is typical, but on the low side, for the sediments of the Mississippi Alabama Florida (MALFA) sand sheet [26]–[29]. Most $CaCO_3$ consist of broken shells.

Gas Content: Dan Albert (University of North Carolina-Chapel Hill) and Dale Bibee (NRL) assessed the likelihood of the presence of free gas in sediments at the experimental site using a combination of direct measurements and modeling. These sandy sediments are low in organic matter

(TOC = 0.30 and 0.77%) and therefore unlikely to produce any methane unless it comes from deeply buried strata or from isolated pockets of higher organic matter. At these water depths, however, there can be significant benthic primary production and thus some potential for generation of oxygen bubbles at the sediment–water interface. Measurement of near surface oxygen production (Albert) and presence of free gas bubbles within the sediment (Bibee) is described below.

Oxygen profiles in surficial sediments were characterized and their responses to fluxes of photosynthetically active radiation (PAR), which mimicked those *in situ*, were measured aboard ship and at a shore-based laboratory using an oxygen microelectrode (Precision Measurement Engineering, Encinitas, CA) inserted into whole cores with a vernier-type micromanipulator (World Precision Instruments, Sarasota, FL). Oxygen microprofiling aboard ship proved difficult because of ship vibrations therefore the sediment cores were transported to laboratory facilities in North Carolina for incubation experiments. In the upper 1 m of the water column midday photosynthetically active radiation (PAR) exceeded 1000 μE·m^{-2}·s^{-1}, but at the bottom that was reduced by $> 90\%$ to about 70 μE · m^{-2} · s^{-1}. Up to seven layers of screening were used to keep light levels below this during the incubations.

There is a very active photosynthetic community in these sandy sediments. Divers noted substantially higher organic material in the shallow troughs of the sand ripples than on the crests but there was no visual evidence of highly reflective bubbles on the bottom. Most of the organic matter appeared to be benthic algal biomass. The incubated cores all produced small oxygen bubbles (<1-mm diameter) at the surface by mid morning in spite of the fact that the average PAR they were exposed to was probably 1/3 to 1/2 of what they were exposed to *in situ*. Oxygen penetration into the sediment more than tripled during the active photoperiod (Fig. 18) from about 1.5 mm in the early morning to >5 mm by late afternoon. Modest supersaturation occurred in the upper millimeter of sediment and in the water just above the sediment. The bubbles that formed adhered to thin, 1–2-mm-long filaments that protruded from the sediment. Due to working at atmospheric pressure, instead of *in situ*, the formation of oxygen bubbles at the sediment surface could not be suppressed. However, bubble formation *in situ* would require much higher oxygen concentrations, which would have to build up against very steep diffusive gradients. Based on the laboratory incubation experiments, we could not directly quantify *in situ* oxygen profiles or assess the risk of reaching saturation and, thus, bubble formation.

Future work will involve computer-modeling simulations to determine if bubble formation appears feasible at these sites. An advection-diffusion-reaction model will be used [51], [52] in which flux of PAR to the sediment surface, photosynthetic efficiency and depth distribution of photosynthesis can be varied to predict what conditions are required to produce gaseous oxygen under *in situ* pressures.

Gas content was measured aboard ship (Dale Bibee, NRL) from three sediment cores sealed at the seafloor by divers. Core tubes are 30 cm long with 5-cm inside diameter and a sharpened edge on the bottom and are sealed with a valve fitting on top. Divers insert the tube into the sediments by hand with the valve

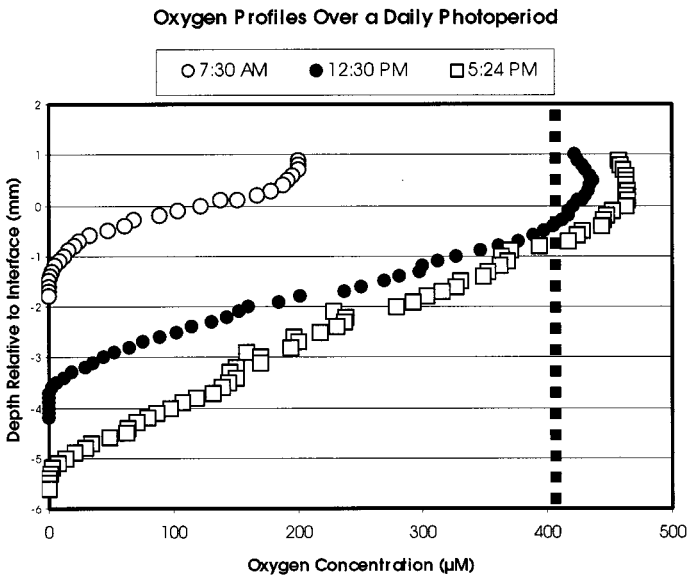

Fig. 18. Oxygen profiles in a sandy core from 18-m depth measured by a microelectrode at various times of day. The dashed line represents oxygen supersaturation.

open and then close the valve to immobilize pore fluid flow within the core. Divers dig out the bottom of the core, and cap it with a gland-sealed pressure cap. The core tube is placed into a clamp and pressure vessel on the seafloor. A tube connects the top of the core with an external port on the pressure case cap. The pressure vessel is returned to the surface.

Once aboard the ship, ports on the pressure vessel are connected to a fluid-filled manifold system. One port hydraulically connects the manifold to the core sample through the tube described above. The other port connects the manifold to water inside the pressure vessel and surrounding the core sample. The manifold is pressurized to seafloor conditions, and valves to the core and confining fluid are opened. As pressure is increased (approximately 200 kPa) in the manifold and the amount of water flowing into the core sample is monitored. Since the confining pressure on the core is equalized to the internal pressure, no expansion of the core tube takes place. Water flow into the core is the result of compressibility of the core sample. Since the sediment and water have small compressibility compared to gas, volume change observed is mostly controlled by the amount of gas in the sediment. Measurements are also collected as the sample is returned to seafloor pressures and data are considered reliable if the volume change is reversible.

The fractional volume of gas ranged between 0.000 02 and 0.000 15 for cores collected near from the stern (0.000 08) and port (0.000 02) sides of the R/V Seward Johnson, and near the BAMS tower (0.000 15). All of these values indicate smaller volumes of gas than the system is designed to resolve. We cannot on the basis of these data reject the hypothesis that the gas content is zero. However, these data constrain the amount of gas to $< 0.000\,15$ volume fraction.

B. Pore Water Salinity and Viscosity

Bulk interstitial pore water samples (10 cc) were collected at 30 cm below the sediment-water interface using a diver-oper-

ated syringe (Richardson, NRL). Salinity was measured using a refractometer and pore water viscosity measured using the Dj-Scientific AV-250 hand-held viscometer calibrated with Copenhagen seawater. Neither the salinity (34–35 ppt) nor the pore water viscosity (range 0.95–1.15 cP) differed significantly from concurrent water samples collected just above the seafloor. Differences in pore water viscosity were controlled by water temperature.

VII. Seafloor Physical and Geoacoustic Properties (in Situ)

In-situ measurement of sediment properties yields the best estimate of undisturbed bulk porosity, density, permeability, and acoustic sound speed and attenuation. Mean values, gradients, and spatial variability of these physical and geoacoustic properties are required to make predictions of acoustic scattering, propagation, and penetration.

A. Geoacoustic Properties

Acoustic properties of the sediment were characterized by several methodologies in order to ascertain spatial variations in sediment compressional and shear wave speed and attenuation. Measurements were made at discrete vertical increments with single or paired probes as well as at varied geometries with tomographic probes and surface mounted arrays. Geoacoustic properties were measured over a wide frequency range in order to understand and predict the importance of sound speed dispersion for acoustic scattering and penetration.

Incremental Measurements: Speed and attenuation of compressional and shear waves were measured with the latest version of the In Situ Sediment geoAcoustic Measurement System (ISSAMS) [53] (Richardson, NRL). ISSAMS is a remotely operated, hydraulic platform that allows fixed, mounted geoacoustic probes to be driven into the sediment at precise depths. Live video is used to monitor probe deployment and to provide visual information on seafloor type. Water conductivity, pressure, and temperature are measured concurrently to calculate bottom water sound speed. Additional probes measure sediment conductivity and penetration resistance. Compressional and shear wave speed and attenuation are measured over pathlengths ranging from 30 to 100 cm and at depths up to 30 cm below the sediment–water interface. For typical compressional wave measurements, transmitted 38-kHz pulsed sine waves are used and time delays and voltages are measured to determine values of speed and attenuation between identical radial-poled ceramic cylinders. Speed is calculated by comparison of received signals transmitted through the sediment with those previously transmitted through seawater overlying the sediments [53]. Shear wave speed is calculated from time-of-flight between bimorph bender elements mounted in flexible, silicone-rubber mounts and driven at near 1.0 kHz. Distances between shear transducers are measured center-to-center between the bender elements before and after deployment. Attenuation of compressional and shear waves ($\mathrm{dB{\cdot}m^{-1}}$) is measured using the transposition technique described by Richardson [53]. An additional set of compressional wave measurements was made over a frequency range of 5–100 kHz using 1–3 piezocomposite transducers.

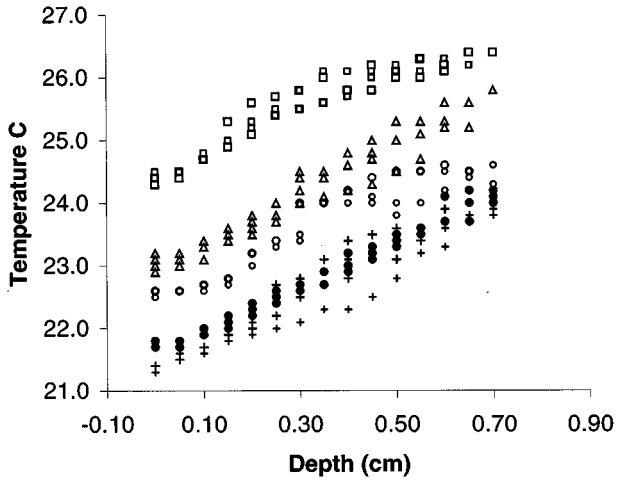

Fig. 19. Gradients of sediment temperature measured by divers during SAX99. Temperature profiles were collected on 22 October (□), 26 October (△), 29 October (○), 5 November (•), and 7 November (+) 1999.

Compressional wave speed (mean: 1739 $\mathrm{m{\cdot}s^{-1}}$, range: 1708–1771 $\mathrm{m{\cdot}s^{-1}}$) and attenuation (mean: 12.7 $\mathrm{dB{\cdot}m^{-1}}$, range: 8.6–17.2 $\mathrm{dB{\cdot}m^{-1}}$) as well as shear wave speed (mean: 120 $\mathrm{m{\cdot}s^{-1}}$, range: 92–147 $\mathrm{m{\cdot}s^{-1}}$) and attenuation (mean: 30 $\mathrm{dB{\cdot}m^{-1}}$, range: 21–40 $\mathrm{dB{\cdot}m^{-1}}$) at the experimental site are typical for sandy substrates [21], [53], [54]. Shear wave speeds show a slight increase with depth (113 $\mathrm{m{\cdot}s^{-1}}$ at 10 cm, 121 $\mathrm{m{\cdot}s^{-1}}$ at 20 cm, 129 $\mathrm{m{\cdot}s^{-1}}$ at 30 cm) whereas no statistical relationships with depth are found for values of compressional wave speed or shear and compressional wave attenuation.

Electrical resistivity (inverse of sediment conductivity) of the sediments was measured concurrently with the sediment geoacoustic properties during 12 deployments (6 sites) of the ISSAMS system. Electrical resistivity is expressed as Formation Factor (ratio of the pore fluid resistivity to the sediment resistivity), a pore-fluid-independent property of the seafloor [55]. Measurement of resistivity of the bottom water as a proxy for pore fluid resistivity is justified by the similarity in pore fluid and bottom water salinity and viscosity. No corrections have been made to account for the difference in temperature (1 °C–2 °C) between the overlying water column and pore water (Fig. 19). Values of formation factor range between 2.8 and 3.7 (mean 3.2) with no statistical difference among the three depth increments (10, 20, and 30 cm) where sediment conductivity was measured. These results suggest a lack of a sediment porosity gradient, which is in concordance with laboratory measurements of porosity (Fig. 16).

In situ shear strength was measured with a quasistatic cone penetrometer attached to the ISSAMS frame. Profiles of penetration resistance of an ASTM standard cone (60° cone with 10 $\mathrm{cm^2}$ area) are measured in the upper 60–70 cm of sediment using a silicon strain gauge bridge pushed into the sediment at a constant rate (1–2 $\mathrm{cm\ s^{-1}}$) by a chain drive [56]. Strain gauge voltages are converted to penetration resistance by comparison to a calibrated load cell. For most of the 26 profiles, the force required to push the cone into the sediment increases rapidly from

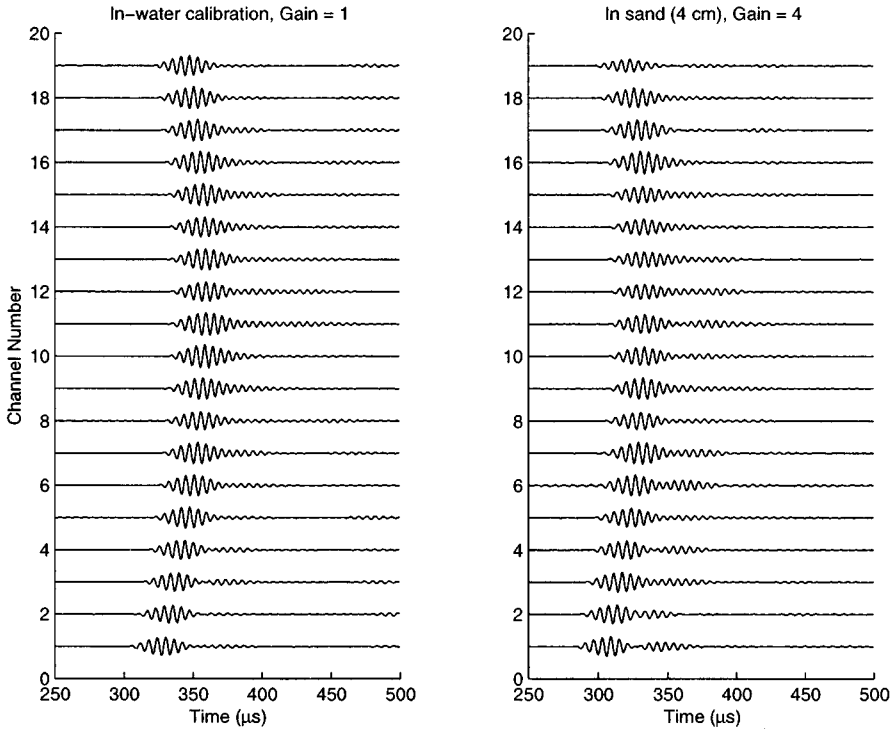

Fig. 20. Selected received signals from 19 channels of data from the high-resolution sediment acoustic imager (AI) measured at 4 cm depth in the sediment. On the left are calibration data, on the right are data taken in sediments. Note the in-sand data has a gain of 4. The arc formed by the 19 arrival times is the result of different path lengths between the source and the receivers. The later arrivals are due to scattering. Differences between these and the remaining 1200 data sets provide the basis of tomographic imaging analysis.

25–50 psi near the surface to 600–700 psi at 60 to 70 cm below the sediment surface.

Acoustic Tomography: The high-resolution sediment acoustic imager (AI) consists of 60 transducers arranged in a circle 25 cm in diameter (D. Tang, APL). Its working principle is similar to that of a medical CT scanner and the system is capable of obtaining 3-D images of sediment sound speed and attenuation coefficient with a spatial resolution of 2 cm (voxel size). This is achieved by successively imaging 2-D horizontal circular sections as the system is pushed into the sediment. During SAX99, a maximum penetration depth of 12 cm was achieved at the four sites imaged. The AI system was also deployed at a fixed position for three days with images collected every 60 s to assess possible temporal changes in sound speed due to biological activity. These data sets (Fig. 20) will be processed to obtain sediment sound speed and attenuation images.

A diver-portable geoacoustic tomographic system was used by Dale Bibee (NRL) to make acoustic measurements in the immediate vicinity of diver-collected gas cores. The system consists of two stainless steel probes, each 1.6 cm in diameter and 60 cm long. Embedded in each probe are eight piezoceramic transducers spaced at 6.5-cm intervals along the probe. Both probes are rigidly mounted to a nylon plate at a spacing of 28 cm. Two small electronics housings are also mounted to the plate and contain the drive power amplifier for one probe and the receive pre-amplifiers and multiplexing for the other. A data acquisition and recording system is contained in a separate pressure vessel that is approximately 23 cm in diameter and 55 cm long. The entire system weighs only a few pounds when submerged so that a diver can move, position, and insert the probes into the seafloor.

In operation, one of the transducers on the source probe is activated with a short tone burst and one of the transducers on the receive probe is amplified, filtered, and routed to a 2.5 MHz, 12-bit digitizer. Full waveforms from 64 to 128 pings are recorded on optical disk for each transducer pair for stacking in subsequent processing. All 64 pairs of transmit/receive transducers are sampled sequentially so that many intersecting paths are produced allowing a tomographic analysis of a 2-D vertical slice of the sediments. The transmitted tone burst consists of 4 cycles of a target frequency. A primary resonance of the transducers is near 300 kHz but a substantial signal can be observed at subharmonics of that frequency. The complete set of transducer pairs is sampled at target frequencies of 312, 156, 78, and 38 kHz. Because the efficiency of the transducers is poor at 38 kHz, and because the tone burst is actually a square wave, significant high-frequency harmonics are also generated when 38 kHz is targeted.

Because of seawater leakage problems in the drive electronics package, only two successful deployments of the system were conducted during SAX99, one near the TAPS tower and one near the Seward Johnson. Fig. 21 shows the velocity–depth data derived from the 150-kHz pulse as measured on horizontal paths between equivalent transducers on the probes. The results are remarkably uniform, with depth fluctuations approximately equivalent in magnitude to the resolution of travel time. There is no evidence for a significant compressional wave speed gradient from these data. Future processing will allow a comparison of wave speed at different frequencies and a reporting

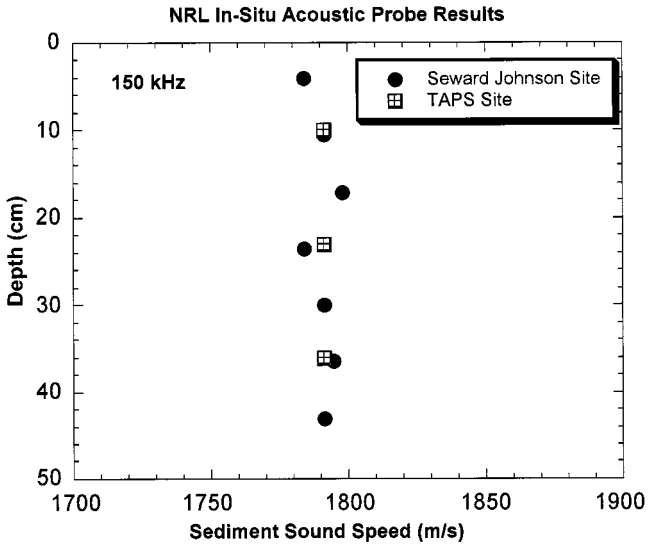

Fig. 21. Sound speed measured at 150 kHz using the NRL high-frequency tomographic system.

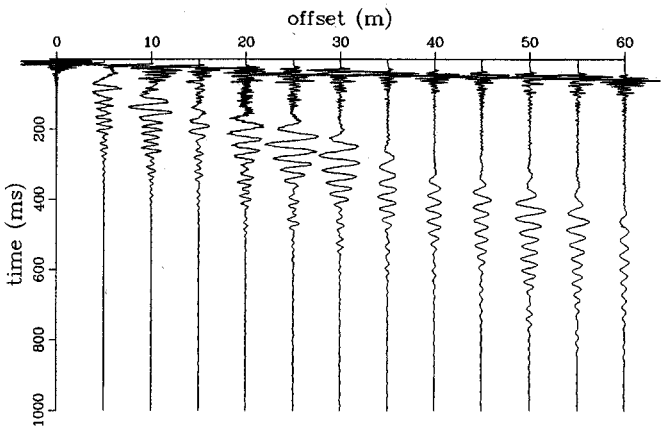

Fig. 22. Typical travel-time curves for one shot using the Lamont-Doherty sled. Each record has been normalized to its maximum amplitude.

of compressional wave attenuation. A tomographic travel-time inversion can be performed on the data, but the initial evidence for uniformity of the sediment suggests that this analysis will yield little new information.

Low-Frequency Acoustic Measurements: Evaluation of mechanisms for penetration of acoustic energy into and scattering from the seafloor requires a realistic frequency dependent model for acoustic propagation through sediments. Values of sound speed and attenuation measured at high acoustic frequencies either *in situ* or in the laboratory are often incorrectly used to predict impedance of the seafloor for low frequency acoustic experiments [7]. Various visco-elastic [15], [17] and poro-elastic models [16], [18] have been used to predict frequency-dependent propagation in marine sediments. One difference between these models is that porous media models predict the existence of two types of compressional waves, the traditional compressional wave and a "slow" wave that attenuates more rapidly. In addition, the porous media model incorporates attenuation mechanisms related to pore fluid motions resulting in a significant frequency dependence of compressional wave speed and attenuation. One visco-elastic model [17] assumes attenuation due to relaxation processes, which are described as a linear function of frequency with minimal wave speed dispersion. This difference has a significant effect on the acoustic penetration and scattering mechanisms not only because of the slow wave, but because a dispersive wave speed in the sediment results in a frequency-dependent critical angle [7]. The demonstrable uniformity of the sediment environment in the SAX99 experiment provided the opportunity to measure sound speeds and attenuations at several scales (and frequencies) without large changes in material properties. A series of low-frequency (10–1000 Hz) measurements are described below.

a) Lamont-Doherty low-frequency experiments: Experiments carried out by Lamont-Doherty Earth Observatory (LDEO) of Columbia University (Bob Stoll) were designed to establish a lower frequency response for the first few meters of sediment. Experiments involved deployment of a linear array of gimbaled, vertical geophones and an impulsive source mounted on a self-righting sled [56]. In unconsolidated sand, sediment sound speed is faster than the overlying water sound speed and increasing overburden pressure causes a small increase in sound speed with depth. As a result very shallow "diving" waves usually produce the first motion observed at the geophones and the travel time versus distance curve based on first arrivals is inverted to obtain p-wave velocity. In addition to the p-wave motion, the impulsive source also generates strong, dispersive interface waves (Scholte waves) that may be analyzed to obtain shear wave speed and attenuation to a depth equivalent to about one wavelength [56], [57].

The travel-time record shows both the first arrivals of the p-wave and the slower dispersive interface wave (Fig. 22). Interface wave inversions are used to obtain depth dependent speed and attenuation by first determining the group or phase velocity dispersion curves of the surface wave and then determining in an iterative manner a layered model that produces matching curves (e.g., see [57]). P-wave speed is determined from shots taken using the higher sampling rate. Each channel is scanned to determine the time of first arrival and a polynomial travel-time curve is derived from a least squares fit to these points. Preliminary analysis of the p-waves returns yields sound speeds near 1600 m·s^{-1} over a frequency range of 50–200 Hz.

b) NRL low-frequency experiments: The NRL low-frequency experiments (Dale Bibee) were similar in concept to those of LDEO, but differed significantly in implementation. A six node linear array of receivers with 3-m spacing was deployed at offsets of 3–60 m from a seafloor acoustic source. Each receiver consisted of a 3-axis geophone package that was buried just below the sediment surface by divers using a water jet system. A hydrophone was deployed on the seafloor adjacent to each node. While lacking the mobility of the LDEO system, the measurements of motions on multiple components is highly desirable for identifying the propagation path of the acoustic signals and isolating the proper signal for study. Burial of the sensor node increases the fidelity of the recording. Data from all of the nodes was cabled to a seafloor pressure vessel containing programmable gain amplifiers, filters, a digitizing system (16 bit), and a digital communication link to the ship.

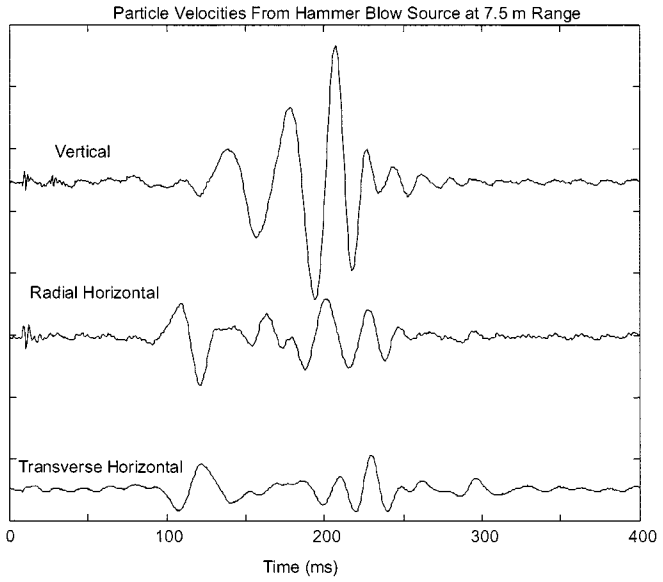

Fig. 23. Three-component measurements of particle velocity resulting from a vertical hammer blow to a steel plate 7.5 m from the receiver. All traces are plotted at the same gain. The small high frequency arrival at a few milliseconds travel time is the compressional wave. The larger low-frequency arrival at later time is a seismoacoustic surface wave. The second high-frequency arrival on the vertical component is a reflection from the sea surface.

Two sources were used to generate seismoacoustic signals on the seafloor. A square steel plate (0.5 m) was placed by divers at several distances (3–12 m) from the receiving array and hit with a large hammer. Divers measured the distance of each source placement from the array with a tape measure and the source time was measured with an accelerometer. The second source was a small (32 ml) airgun mounted to a steel plate and fired at a pressure of 6.7 MPa. The peak frequency of this bubble was near 70 Hz, but significant energy was produced at harmonics of this frequency throughout our band of interest. A hydrophone was mounted on the plate approximately 20 cm from the airgun ports to measure the source timing and signature. Fig. 23 shows data recorded at one of the nodes for a hammer blow at a distance of 7.5 m. As in the LDEO data, an initial compressional wave signal is seen followed by a lower frequency dispersed surface (Scholte) wave. The vertical component signal is dominated by the fundamental mode Scholte wave while the horizontal components display substantial energy in the earlier arriving higher order modes. The compressional wave signal is most clearly seen on the horizontal radial seismometer. Inversion of phase velocity dispersion in the fundamental-mode Scholte wave results in a shear speed depth profile which is remarkably consistent with the predictions for unconsolidated sands [58], [59]. An analysis of the compressional wave signals from airgun shots propagating across the array indicates that the speed is between 1550 and 1600 $\mathrm{m{\cdot}s^{-1}}$. While the particle motions for this phase are predominantly horizontal as expected, the initial vertical motion is upward indicating that the signal is propagating through the sediment rather than the water. These data are consistent with the analysis of the LDEO data.

c) Scripps low-frequency experiments: To take advantage of airgun signals generated as part of the NRL experiments, Mike Buckingham from Scripps Institution of Oceanography (SIO) deployed a short vertical hydrophone array at various distances from the airgun source. The vertical array of four ITC 8233 hydrophones [60] was deployed from a small motorboat and suspended at a depth of approximately 10 m. The sensors were positioned at 0, 0.33, 1, and 2.33 m above the bottom of the array, and the time series from the four elements were recorded on two separate (nonsynchronized), two-channel Sony TCD D8 DAT recorders (20 kHz band width). In effect, this arrangement split the four-element array into two independent, coherent, two-element arrays.

Fifteen airgun shots were recorded at various receiver locations as the array drifted in the current and the source remained fixed on the seafloor approximately 1 km distant. A small tilt sensor positioned near the top of the array provided the angle of inclination to the vertical, but not the direction of tilt. Overall, the experimental arrangement was similar to, but on a smaller scale than, that recently employed by Godin *et al.* [61], who used a 16-element, 225-m vertical array to record head waves produced by explosive sources.

The received signal at each sensor consisted of three easily identifiable components: the direct water-borne wave and two distinct precursors. The difference in arrival times between the water wave and precursors, together with known source–receiver separations measured with DGPS equipment, allowed calculation of the average of the horizontal component of sound speed. Range dependence of this speed identified the first arrival as a diving wave. The data are consistent with a seabed where sound speed increases with depth by 3.5 $\mathrm{m{\cdot}s^{-1}}$ per meter and the surficial sediment sound speed of 1600 $\mathrm{m{\cdot}s^{-1}}$. It should be noted that these diving waves are likely to have penetrated approximately 200 m below the seafloor, restricting their relevance to the acoustics of the sediment layer. The second precursor, greater in amplitude than the diving wave arrival, showed no range dependence in sound speed and is consistent with an interface head wave traveling at approximately 1620 $\mathrm{m{\cdot}s^{-1}}$.

d) Synthesis of low-frequency results: Analysis based on only a small amount of the total data set indicate the low-frequency compressional wave speeds derived from the NRL, Scripps and LDEO experiments ($\sim$ 1600 m/s) are significantly lower than the high-frequency (50–400 kHz) estimates (1750–1790 m/s) measured using *in situ* probe and laboratory core measurements. This velocity dispersion is consistent with the Biot theory (e.g., [16]) that predicts significant velocity dispersion in unconsolidated sands over an intermediate frequency range (typically about the 1–10-kHz range, but shifting upwards as permeability decreases). This result has important implications when determining the critical angle (or pseudo-critical angle) for low grazing angle studies.

B. In Situ Permeability

Two investigators measured sediment permeability using devices consisting of fritted probes driven into the sediment either mechanically or manually.

UW Physical Properties Tripod: The University of Washington (Paul Johnson UW) Physical Properties Tripod was utilized with an *in situ* probe designed by SEAPROBE, Inc.,

(Richard Bennett) to measure sediment permeability in the upper 50 cm of the seafloor. A constant volume-constant flow pump delivered calibrated over-pressured filterer seawater into the surrounding sediment through a calibrated porous stone while continuously monitoring the fluid output with a pressure transducer. The fluid flux through the porous stone increases the sediment pore pressure field and the selectable constant flow rate and constant pressure measurements provide a measure of sediment permeability after corrections are made for temperature and for probe impedance (probe permeability). A field calibration of the probe was obtained in seawater using different flow rates and fluid pressures. This procedure provides reliable data on the functioning of the probe prior to each insertion and establishes a value for the permeability of the probe.

The tripod and permeameter were deployed at 19 stations in the vicinity of the SAX99 experiments. Intrinsic permeability values varied between 0.3 to 6.2×10^{-11} m^2 (approximately 0.3 to 5.4×10^{-2} cm$\cdot$ s^{-1} in units of hydraulic conductivity) with a general decrease in permeability with depth in the sediment (upper 50 cm). These values are in agreement with laboratory measured values of intrinsic permeability reported in this paper (1.8 to 5.1×10^{-2} cm$\cdot$ s^{-1}) and are reasonable for sandy sediment.

NRL Permeameter: Sediment permeability was measured in sediments directly under the anchored Seward Johnson using the NRL (Dawn Lavoie) in-situ permeameter. This system is based on the falling head design of Bennett *et al.* [62]. The *in situ* Darcy's coefficient of permeability (hydraulic conductivity) ranged between 0.99–1.23×10^{-3} cm$\cdot$ s^{-1} (approximately 10^{-12} m^2 in units of intrinsic permeability) at depths between 36 and 66 cm below the sediment surface. Sediment disturbance, a result of too high flow rates, eliminated measurement of permeability in sediment depths shallower than 35 cm.

C. Sediment Resistivity

Sediment electrical resistivity was measured with probes intruding into the sediment and with a nonintrusive array of electrodes resting on the sediment surface. The three intrusive methods involved collection of independent, single vertical profiles or a multiple array of closely spaced, vertical profiles.

In Situ Resistivity Probes: A conductivity (inverse of resistivity) probe was utilized on ISSAMS to measure the near-surface values of sediment resistivity at three depth increments (see Section VI-A1). Values of Formation Factors (ratio of pore water to sediment conductivity) ranged between 2.8 and 3.7 (mean 3.2) with no statistical difference among the three depth increments (10, 20, and 30 cm). These results suggest a lack of gradients in sediment porosity.

Resistivity profiles were collected using a diver-deployed probe (IRP: *in situ* resistivity profiler) at 10 different sites within the study area (Rob Wheatcroft, OSU). A total of 66 profiles were collected. Profiles were typically 120 mm long with a vertical sample spacing of 0.25 mm. A roughly equal number of profiles were obtained on ripple crests, ripple troughs and biogenic mounds. Analysis to date reveals subtle differences in the near-surface porosity between these three bottom types, but no substantial between-site variation within the study

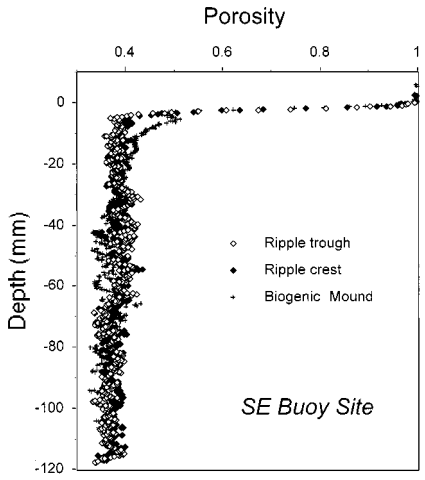

Fig. 24. Representative porosity profiles obtained using a diver-deployed IRP (Wheatcroft, OSU). Note the higher porosity in the upper 10 mm of the seabed under the biogenic mound.

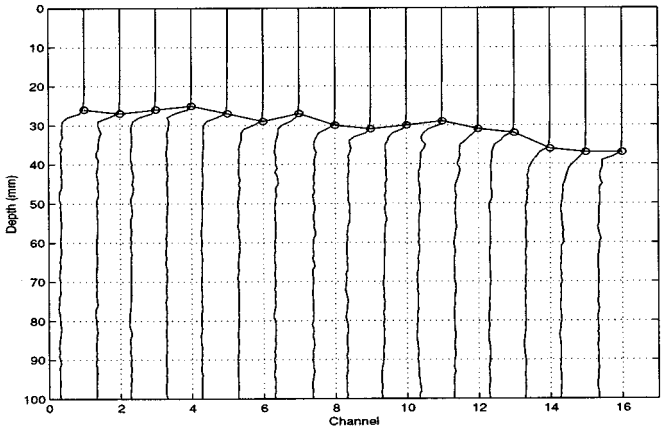

Fig. 25. Gradients of sediment conductivity measured with the IMP multisensor conductivity probes system designed by APL-UW. Gradients are measured at 1-cm spatial resolution for 16 channels. The curve linked by the circles is the inferred water–sediment interface. Data points above the curve are from the water column; below it are data from sediments.

area. Porosity profiles representative of the experiment site are shown in Fig. 24. At sediment depths from 90 to 110 mm the Formation Factor ranged from 3.08 to 3.78 and had a standard deviation of 0.13.

The *in situ* measurement of porosity (IMP) is a multisensor conductivity probe system mounted on a self-contained frame with a vertical and a horizontal drive mechanism (D. Tang, APL). A major improvement of the IMP over other types of conductivity devices is that the IMP takes a 3-D matrix of data points in the sediments, therefore, providing data sets which can be used to estimate power spectra of sediment conductivity or calculated sediment density or porosity. The system makes sediment conductivity measurements over a volume that is 100 cm long, 15 cm wide, and 15 cm deep. The spatial resolutions of the measurements are 1 cm in the horizontal dimensions and as small as 0.1 cm in the depth dimension. Fig. 25 demonstrates both gradients and volume heterogeneity of sediment conductivity at the SAX99 experimental site. Except for few outliers, values of Formation Factor ranged from 3.17

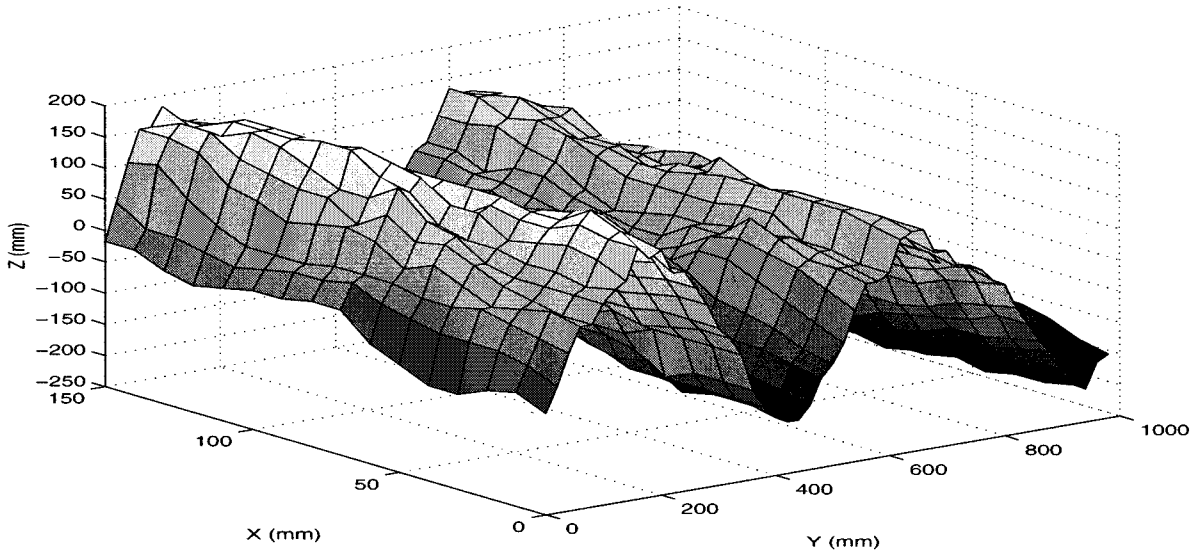

Fig. 26. Bottom roughness based on the inferred water–sediment interface measured with the IMP multisensor conductivity probes (see Fig. 25). Note scales for difference dimensions are not the same.

to 3.34 with a standard deviation of 0.14. Two-dimensional bottom roughness is also determined from successive profiles of electrical resistivity (Fig. 26) and will be used to estimate interface roughness spectra.

Electrode Array: A diver-operated resistivity array has been developed by the British Geological Survey (Peter Jackson) for imaging the fine-scale structure of the topmost 100 mm of the seabed. The technique uses a grid of 256 electrodes (16×16) spaced 10 mm apart to inject current while simultaneously measuring series of potential differences. This approach enables 3840 individual measurements to be made during a 90-s scanning sequence. Current is passed separately through each individual current electrode in turn, enabling a wide variety of depths of investigation to be employed. Subsequently, these measurements are inverted into resistivity values using a smoothness constraint and a 3-D forward model. Formation Factors are calculated using the resistivity of the seawater immediately above the measuring site. Approximately 100 scans have been made and it is planned to combine adjacent ones into larger maps to achieve greater coverage.

An example of preliminary processing is shown in Fig. 27. The Formation Factor values are in the range 2–5, consistent with small-scale heterogeneity created by bioturbation in the sandy sediments. The average value of Formation Factor of the top 75-mm depth interval is 3.8, with some evidence for Formation Values in excess of 5.0 at the greatest depths. Sediment resistivity is controlled by fluid chemistry, porosity, and particle shape and is therefore suitable for further interpretation in terms of tortuosity providing basic geotechnical properties have been established by core sampling [63]. Because it is noninvasive, this method has the potential to characterize unstable 3-D inhomogeneities, such as created by bioturbation, which may be altered using invasive approaches.

Comparison of Sediment Resistivity Measurements: Average *in situ* values of sediment resistivity/conductivity measured by ISSAMS at are slightly lower (Formation Factor mean 3.2; range 2.8–3.7) than reported by Peter Jackson (FF: mean 3.8; range 2–5) but similar to those measured by DJ Tang (FF: mean 3.25; range 3.17–3.34) and Rob Wheatcroft (FF: mean 3.4; range 3.1–3.8). Differences in techniques including the effects of sediment disturbance, artificially created pathways along invasively inserted probes, and voxel size need to be investigated to account for these differences.

VIII. Sediment Microstructure

Small-scale structure of sediment (microfabric), including grain and pore space spatial relationships, control sediment physical, geotechnical, and geoacoustic properties. In order to model acoustic propagation in porous media, parameters, such as, permeability, tortuosity, pore size distribution, density, and porosity, need to be quantified. The effect of spatial heterogeneity on sediment properties and behavior, at these small scales, also needs to be quantified either through deterministic models or the use of statistical characterization of microfabric parameters. Fine-scale characterization of sediment microfabric was made with X-ray computed tomography and microscopic examination of unaltered and resin-impregnated sediments.

A. Resin Impregnation and Analysis of Sediment Structure

Dawn Lavoie and Allen Reed (NRL) quantified relationships among pore network properties (pore dimensions, pore size distribution, connectivity, coordination number, and tortuosity) and grain properties (shape, surface morphology, orientation, specific surface area, and grain–grain contacts) using image analysis techniques. They used these data to quantify relationships between fluid flow and sediment microfabric and to provide input for acoustic propagation models. Sampling techniques were employed to minimize sediment disturbance, which allows quantitative characterization of *in situ* grain–pore relationships.

The pore and grain relationships were preserved in diver-collected cores and *in situ* sediment samples using standard vacuum impregnation techniques and resin impregnation with

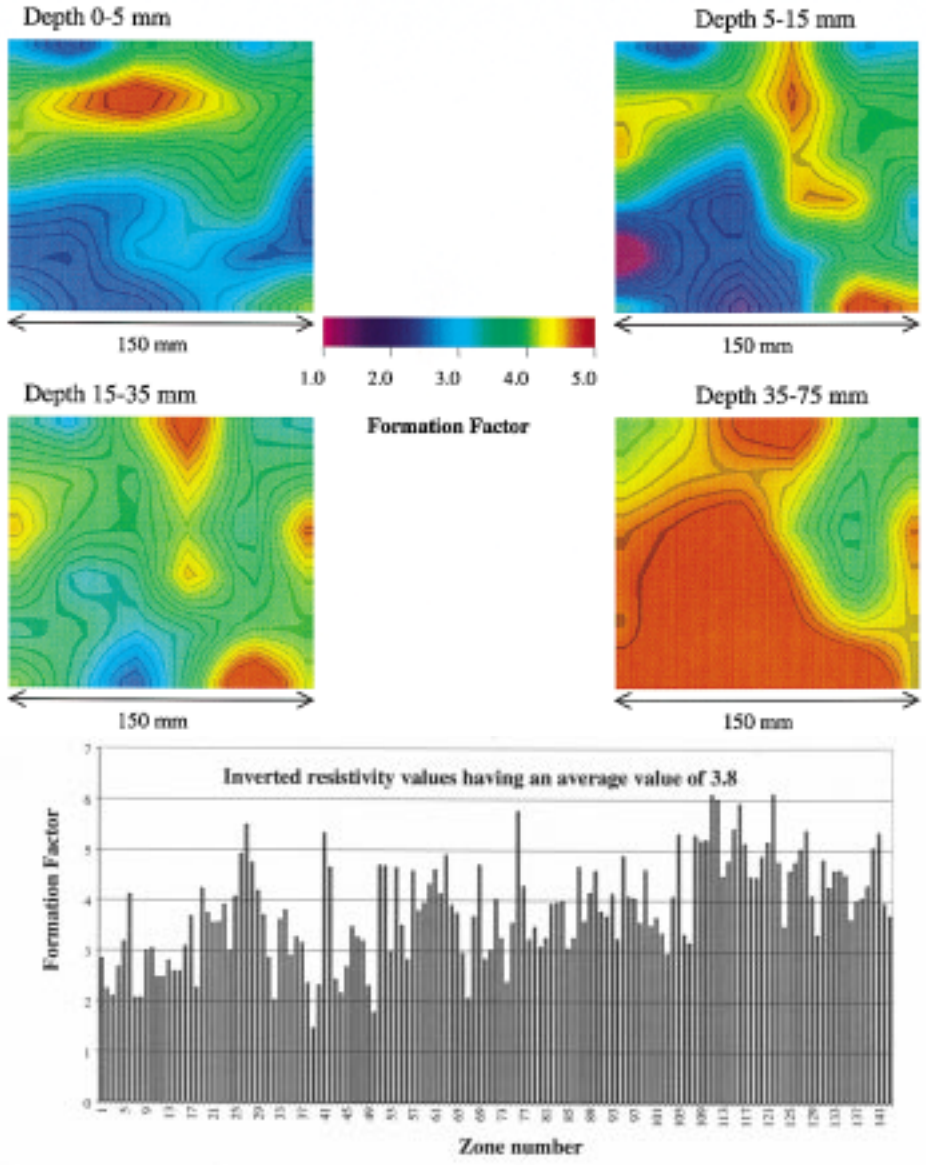

Fig. 27. An example of processed (preliminary) resistivity data showing plan tomograms at four gradually increasing depth intervals. Data collected with a diver-deployed resistivity array (Peter Jackson, BGS).

an *in situ* embedding device (ISED) (Fig. 28), respectively. Sediments were subsampled and imaged to evaluate homogeneity, isotropy, and pore geometry at a high resolution ($\sim 10\,\mu$m). Subsample sizes were $\sim$ 4 cm^2 cross-sections for imaging with scanning electron microscopy (SEM) and $\sim$ 0.8 cm^3 volumes for characterization using computed tomography (CT) (Figs. 29(a) and 30). Images techniques were used to quantify pore parameters (i.e., throat lengths and widths, body radius, and porosity) [see Fig. 29(b) and (c)]. Effective medium theory technique (EMT), which relates pore parameters to fluid flow, was used to estimate a Darcy's coefficient of permeability.

ISED samples were collected from crests and troughs of bedforms near R/V Seward Johnson, near the BAMS tower, and at the APL penetration site. Predictions of permeability ($3.5 \times 10^{-3} \pm 2.3 \times 10^{-3}$ cm $\cdot$ s^{-1}) were midway between values of permeability reported by Briggs (18 to 51×10^{-3} cm $\cdot$ s^{-1}) and Bennett (3 to 54×10^{-3} cm $\cdot$ s^{-1}) and those measured by Lavoie ($\sim 1.0 \times 10^{-3}$ cm $\cdot$ s^{-1}). The ISED cores were also cut into ~ 2.5-cm-thick sections and X-rayed to evaluate cm-scale homogeneity. Based on visual observation sediments are mostly fine sand overlying a slightly coarse layer with more abundant shells which occurs at depths > 5 cm.

B. Computed Tomography

Sediments are being examined via X-ray computed tomography (Tim Orsi, PSI) to develop acoustically relevant descriptions of sediment continuum and discrete scatterer characteristics within the study area[64], [65]. Divers collected five short cores from two sites: the first site was located 30 m west of the NW buoy and the second site was proximal to the SW buoy. For this analysis, we are using a Universal 2060 CT scanner following the approach outlined by Orsi [66]. The cores were scanned every 3 mm, using a 2-mm-thick X-ray beam. Each scan produces a 512×512 voxel image, with each voxel assigned a value, a CT number, that is directly related to bulk density [67]. The (x, y, z) dimensions of a voxel are 0.25 mm$\times$ 0.25

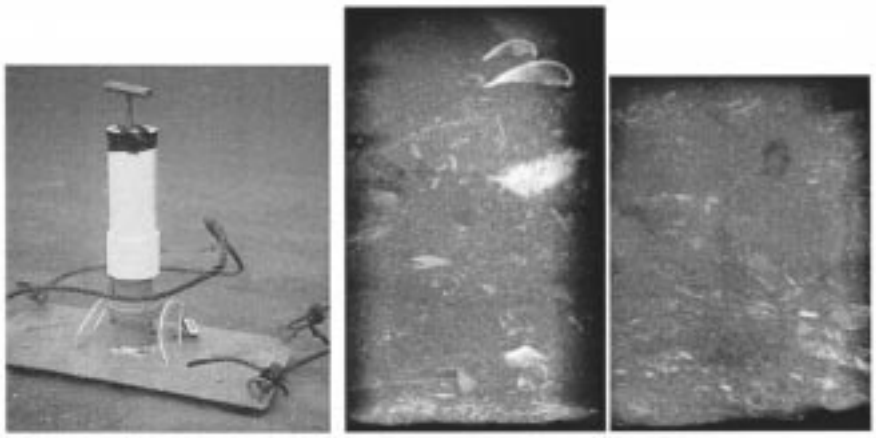

Fig. 28. ISED deployed near the BAMS tower. X-radiographs of ISED cores, which were collected near the Seward Johnson in a ripple crest (center) and a ripple trough (right). (Photos by Ricky Ray).

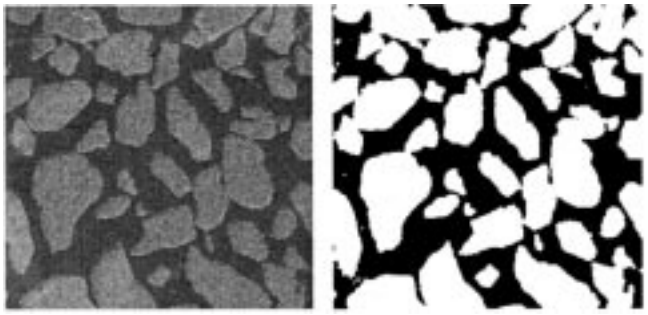

(a) (b)

(c)

Fig. 29. (a) Scanning electron microscopy images were used to analyze pore structure and geometry, by creating (b) an eroded-dilated image and then (c) a Euclidean Distance Map, which enables the quantification of the pore geometry.

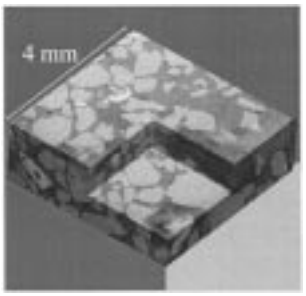

Fig. 30. Volumetric recreation of a 2-D CT image from a sediment sample collected with ISED (image generated by Kirth Simmonds, Naval Research Laboratory).

mm $\times$ 2 mm, representing a sediment volume of 0.125 mm^3. An average of 100 CT images was taken per core.

IX. Biological and Biochemical Processes

Surface roughness, volume heterogeneity, and sediment properties have all been implicated in various hypotheses offered to explain acoustic scattering from the seafloor and the anomalous penetration of sound into the seabed at subcritical scattering angles [1], [2]. Biological processes in coastal seas may affect all of these bottom characteristics.

Benthic animals can affect seabed acoustic properties in a variety of ways. For example, animal burrows and the presence of buried shells and shell fragments are biological sources of volume heterogeneity in the seabed. Infauna can create mounds, depressions, and subsurface layers during burrowing and feeding. Another potential source of biological modification of seabed acoustic properties are so-called "bentho-pelagic" organizms. They spend the daylight hours on or in the seabed, hidden from visual predators. When nighttime light levels are low enough (e.g., during the dark of the moon or when it is cloudy), these animals may emerge from the bottom to feed in the water column. Modern ecological theory, verified in freshwater environments, also suggests that they may come out during lighted periods to feed if the food reward is rich enough. Several species of copepods, mysids, amphipods and shrimp, for example, are known to exhibit this behavior [68], [69]. When such animals emerge from or burrow into the bottom, they alter the small-scale (millimeters to centimeters) topography (roughness). This type of bioturbation, along with bottom currents and surface gravity waves, may reshape bottom contours at larger scales (centimeters to meters) because such animals often travel in large groups. Other biological processes, including bacterial processes, may effectively change material properties of pore water and properties at grain contacts. Exudates of bacteria and other benthic or bentho-pelagic lifeforms may "glue" together grains of sediment, forming local quasi-rigid viscoelastic structures, thereby changing bulk physical and acoustical properties of sediments.

Scientists from BAE SYSTEMS (Van Holliday, Charles Greenlaw and Duncan McGehee), working with Peter Jumars (University of Maine), Liko Self and Jill Schmidt (University of

Washington), and David Thistle and Keith Suderman (Florida State University), conducted manipulative experiments and made a variety of measurements in an effort to detect and quantify the effects of some of these biological processes on sediment properties and behavior. One of the principal thrusts of the BAE SYSTEMS team was to monitor the water column immediately above the seabed for evidence of emergence and reentry of bentho-pelagic animals. Two multifrequency Tracor Acoustic Profiling Systems (TAPS-1 and TAPS-2) were mounted on subsurface moorings with their sound beams aimed downward to examine the water column from the seabed to a height of 6 m. These systems, operating at acoustic frequencies of 265, 420, 700, 1100, 1850, and 3000 kHz, were located in water approximately 18 m deep with a separation of 170 m (Fig. 3). This physical arrangement was intended to provide data that would allow some degree of separation of the effects of light-driven and advective events. TAPS-1 and Taps-2 measured volume backscattering every 6.25 cm or 12.5 cm in depth, respectively. TAPS-X was mounted nearby (Fig. 3) on the seabed acoustically looking up into the water column, and measured volume scattering strengths from the surface to a depth of 1 m above the seabed with a resolution of 12.5 cm. This unit also had a photosynthetically active radiation (PAR) sensor attached to test whether bottom emergence was mediated by ambient light. All TAPS were cabled to a van on the R/V Seward Johnson and data on volume backscattering strengths collected at 1-min intervals were recorded digitally and transmitted to a shore station every hour using a spread-spectrum RF link for near-real-time processing.

A pan/tilt video camera, mounted 3.5 m above the seabed on a tower (Fig. 3), was used in an attempt to observe the behavior of benthic macrofauna (e.g., sand dollars, sea stars). The value of these video observations, however, was limited by the difficulty of resolving the bottom given poor visibility and by the large numbers of fish that collected around the tower, effectively blocking the camera's view.

Preliminary examination of the acoustic records from the three TAPS units suggests that seabed emergence of organizms occurs after sunset (Fig. 31). On 7 November the moon was nearly new, providing optimum conditions for light-mediated bottom emergence of bentho-pelagic organizms. In the late afternoon, a layer of acoustic scatterers at about 5 m above the seabed descended gradually, thickening as it did. Not long before sunset fish collected immediately under the TAPS unit, but then dispersed after dark (this occurred just about every day during the experiment, both at dusk and dawn). Other fish appear to have descended to the seabed at about the same time. Soon after, at about 1830, there was a 10-min intense exodus of smaller acoustic scatterers from the seafloor into the water column. These acoustic scatterers appear to have added considerably to the volume scattering of layer present, which at this point reached from the seabed to a height of 5 m. The small bright spots in the cloud were undoubtedly fish, no longer orienting on either the bottom or the TAPS unit.

Acoustic measurements can resolve bentho-pelagic migration behavior in space and time, but cannot yet be used for species identification. Acoustic sampling was, therefore, supplemented with direct trapping of emergent macrofauna by daily

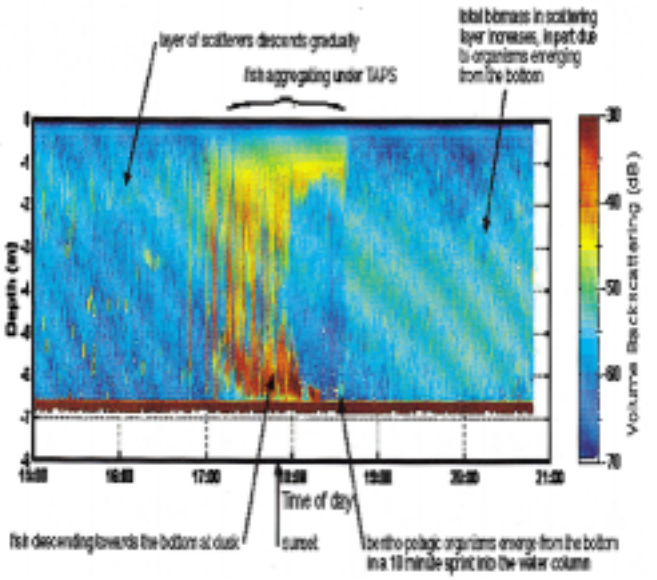

Fig. 31. Preliminary volume scattering strengths at 265 kHz collected from one of the downlooking TAPS units. Measurements were made once per minute over 6 h (1500–2100 CST) during the evening of 7 November 1999. The seabed was approximately 6.5 m below the acoustic sensor.

deploying 1-mm^2, pyramidal traps (1-mm mesh sides) by Liko Self and Peter Jumars. At the top of the pyramid trap is a funnel that narrows to a tube and leads into a collecting jar, much like a minnow trap on its side. Two traps were deployed on each of several nights. A diverse collection of animals, including portunid crabs, was captured, although pelagic mysid and decapod shrimp dominated catches. Contrary to expectation, there was little evidence that the migration was reduced by moonlight, except perhaps at the fullest stages of the moon (Fig. 31).

Emergence is not confined to the macrofauna and megafauna. Animals of sub-millimeter size emerge from the seafloor in great numbers in some habitats. Although this phenomenon has been studied in depths of less than ~ 1 m, its importance on the shelf is unknown. One of Florida State University (Dave Thistle and Keith Suderman) goals was to document the occurrence of sub-millimeter emergers from shelf sands and to identify the emergers. To do so, inverted-funnel traps were used to collect animals that emerged from the sediment and swam > 15 cm above bottom. Although this type of trap works well, it creates still water over the seabed sampled, which is unnatural. To guard against the possibility of artifacts, a similar type of trap with the lowest 4 cm of the trap was open to ambient flow was also used. Between 3 and 12 November 1999, five 24-h deployments of each trap type were accomplished and sediment cores were collected from each area sampled by traps. Preliminary examination of the samples suggests that harpacticoid copepods are important emergers on the shelf, as they are in shallower water.

In order to test effects of emergent fauna on acoustic backscatter from the bottom, Peter Jumars and Liko Self performed experiments designed to exclude these emergent fauna. They created three replicate treatments and three replicate controls in the field of view of each of BAMS and XBAMS (Fig. 3). The treatments consisted of black plastic stretched

over a 2 m $\times$ 2 m frame made of construction rebar and left in place approximately 3 days to suffocate the underlying animals or cause them to leave. Controls were rebar frames without the plastic. Both treatments and controls were smoothed to remove obvious microtopography. The rebar and plastic structures were removed early in the day and their locations monitored acoustically. It was anticipated that no emergers would pockmark the treatment sites at dusk, but that animals would begin to return to these locations at dawn. Data have not yet been analyzed to support this assumption. In addition, the most prominent megafauna of the area were also manipulated. Sand dollars were collected near the SAX study area and concentrated to nearly complete areal cover of the seabed in 1-m^2, plastic-fenced "corrals" (80 per treatment at XBAMS and 105 per treatment at BAMS). Again, three treatments were placed in the field of view of each of BAMS and XBAMS, as were three controls (pens without added sand dollars). Data have not been analyzed.

Less obvious but more pervasive and far more abundant are sedimentary bacteria. Jill Schmidt (University of Washington) assayed bacterial natural abundance and manipulated that abundance to test alternative hypotheses about factors that control sedimentary bacterial abundance and determine the location of bacteria with respect to grain–grain contacts. Manipulations included nutrient additions and exclusion of potential predators. Not only bacteria themselves, but also their visco-elastic mucous secretions, may affect frequency-dependent sediment acoustic behavior.

Two types of samples were collected: 10-cm^3 syringe samples for bacterial abundances and 60-cm^3 syringe samples for embedding. Sediment from 0 to 1 cm sediment depth in the 10-cm^3 samples was extruded from the corer, diluted with particle-free (0.2 μm-filtered) artificial seawater, and fixed with formaldehyde (2% final concentration). These samples were stored at 4 °C in the dark until processed for counting. In the laboratory, bacterial counts were made under epifluorescence microscopy, according to Deming and Colwell [70] and Epstein and Rossel [71]. Bacterial abundances were scaled to dimensions of both wet sediment volume and pore water fluid volume [72]. The larger syringe samples were processed on shipboard using advective replacement of a succession of pore fluids. Care was taken to maintain sediment-grain geometry during this process. Samples were stained with 10-μm 4', 6-diamidino-2-phenylindole (DAPI; Sigma), fixed (10% formalin in artificial seawater), dehydrated via a graded series of ethanol in filtered seawater (from 50% to 100% ethanol), and embedded with Spurr's epoxy resin (Polysciences). Samples were then cured at 70 °C overnight. Sections of embedded cores were first examined under backscatter scanning electron microscopy (SEM) to determine grain and pore geometry. The same fields were then visualized under epifluorescence microscopy and positions of bacteria on grain edges were recorded on the binary images. Image processing algorithms were used to classify habitat (grain-surface area and pore space) based on pore dimensions. Bacteria were then classified according to the habitat they occupied. Image processing will be used to estimate porosity, grain-surface area, and grain-size frequency distributions [73]. Porosity will be measured gravimetrically. The single-point BET N_2 adsorption method will be used to measure N-specific surface area [74].

ACKNOWLEDGMENT

J. Simmen, J. Kravitz, and J. Eckman were the ONR program officers in charge of the DRI. The authors appreciated the excellent support of the captains and crew of the R/V Seward Johnson (Harbor Branch Foundation, Fort Pierce FL), R/V Pelican (LUMCOM, Cocodrie LA), R/V Gilbert (USGS, St Petersburg FL), and R/V Tommy Munro (Gulf Coast Research Laboratory, Ocean Springs MS). The authors thank the numerous other scientists, engineers, divers, and technicians who contributed to the success of these experiments.

REFERENCES

[1] E. I. Thorsos, K. L. Williams, N. P. Chotiros, J. T. Christoff, K. W. Commander, C. F. Greenlaw, D. V. Holliday, D. R. Jackson, J. L. Lopez, D. E. McGehee, M. D. Richardson, J. Piper, and D. Tang, "An overview of SAX99: Acoustic Measurements," *IEEE J. Oceanic Eng.*, vol. 26, pp. 4–25, Jan. 2001.

[2] N. P. Chotiros, "Biot model of sound propagation in water-saturated sand," *J. Acoust. Soc. Amer.*, vol. 97, pp. 199–214, 1995.

[3] J. L. Lopez, "Observations of anomalous acoustic penetration into sediment at shallow grazing angles," *J. Acoust. Soc. Amer.*, vol. 99, pp. 2471–2474, 1996.

[4] J. Osler and A. P. Lyons, "Seabed penetration," in presented at the Conf. on High-Frequency Acoustics in Shallow Water, La Spezia, Italy, June 30, 1997.

[5] N. P. Chotiros, A. M. Mauter, A. Lóvick, Å Kristensen, and O. Bergem, "Acoustic penetration of a silty sand sediment in the 1–10 kHz band," *IEEE J. Oceanic Eng.*, vol. 22, pp. 604–615, 1997.

[6] H. J. Simpson and B. H. Houston, "Analysis of laboratory measurements of sound propagating into an unconsolidated water-saturated porous media," *J. Acoust. Soc. Amer.*, vol. 103, pp. 3095–3096, 1998.

[7] A. Maguer, E. Bovio, W. L. Fox, E. Pouliquen, and H. Schmidt, "Mechanisms for subcritical penetration into a sandy bottom: Experimental and modeling results," *J. Acoust. Soc. Amer.*, vol. 107, pp. 1215–1225, 2000.

[8] A. N. Ivakin and D. R. Jackson, "Effects of shear elasticity on sea bed scattering: Numerical examples," *J. Acoust. Soc. Amer.*, vol. 97, pp. 346–354, 1998.

[9] E. I. Thorsos, D. R. Jackson, J. E. Moe, and K. L. Williams, "Modeling of subcritical penetration into sediments due to interface roughness," in *High Frequency Acoustics in Shallow Water*, N. P. Pace, E. Pouliquen, and A. P. Lyons, Eds: NATO SACLANT Undersea Research Centre, 1997, pp. 563–569.

[10] E. I. Thorsos, D. R. Jackson, and K. L. Williams, "Modeling of subcritical penetration into sediments due to interface roughness," *J. Acoust. Soc. Amer.*, vol. 107, pp. 263–277, 2000.

[11] D. R. Jackson, K. B. Briggs, K. L. Williams, and M. D. Richardson, "Test of Models for high-frequency bottom scattering," *IEEE J. Oceanic Eng.*, vol. 21, pp. 458–470, 1996.

[12] E. I. Thorsos, "Report on the Office of Naval Research High-Frequency Acoustic Workshop 16–18 April, 1996,", Tech. -Rep. APL-UW TR 9702, 1997.

[13] K. L. Williams and D. R. Jackson, "Bottom bistatic scattering: experimental results and model comparision for a carbonate sediment," in *Proc. High-Frequency Acoustics in Shallow Water Conf.*, SACLANTCEN, Lerici, Italy, 1997, pp. 605–610.

[14] D. Chu, K. L. Willaims, D. Tang, and D. R. Jackson, "High-frequency bistatic scattering by sub-bottom gas bubbles," *J. Acoust. Soc. Amer.*, vol. 102, pp. 8006–814, 1997.

[15] E. L. Hamilton, "Elastic properties of marine sediments," *J. Geophys. Res.*, vol. 76, pp. 579–604, 1971.

[16] R. D. Stoll, *Sediment Acoustics. Lecture Notes in Earth Sciences 26.* New York, NY: Springer-Verlag, 1989, p. 152.

[17] M. J. Buckingham, "Theory of compressional and shear waves in fluidlike marine sediments," *J. Acoust. Soc. Amer.*, vol. 103, pp. 288–299, 1998.

[18] R. D. Stoll, "Comments on "Biot model of sound propagation in water-saturated sand [*J. Acoust. Soc. Amer.*, vol. 97, pp. 199–215, 1995]," *J. Acoust. Soc. Amer.*, vol. 103, pp. 2723–2725, 1998.

[19] N. P. Chotiros, "Response to: 'Comments on 'Biot model of sound propagation in water-saturated sand' [*J. Acoust. Soc. Amer.*, vol. 103, pp. 2723–2725, 1998]," *J. Acoust. Soc. Amer.*, vol. 103, pp. 2726–2729, 1998.

[20] M. D. Richardson and D. K. Young, "Geoacoustic models and bioturbation," *Mar. Geol.*, vol. 38, pp. 205–218, 1980.

[21] M. D. Richardson and K. B. Briggs, "In situ and laboratory geoacoustic measurements in soft mud and hard-packed sand sediments: Implications for high-frequency acoustic propagation and scattering," *Geo-Mar. Lett.*, vol. 16, pp. 196–203, 1996.

[22] P. A. Jumars, D. R. Jackson, T. F. Gross, and C. Sherwood, "Acoustic remote sensing of benthic activity: a statistical approach," *Limnol. Oceanogr.*, vol. 41, pp. 1220–1241, 1996.

[23] K. B. Briggs and M. D. Richardson, "Small-scale fluctuations in acoustic and physical properties in surficial carbonate sediments and their relationships to bioturbation," *Geo-Mar. Lett.*, vol. 17, pp. 306–315, 1997.

[24] J. Mazzullo and M. Peterson, "Sources and dispersal of late Quaternary silt on the northern Gulf of Mexico continental shelf," *Mar. Geol.*, vol. 86, pp. 15–26, 1989.

[25] J. C. Ludwick, "Sediments in the northeastern Gulf of Mexico," in *Papers in Marine Geology, Shepard Commemorative Volume*, R. L. Miller, Ed. New York, NY: Macmillan, 1964.

[26] L. J. Doyle and T. N. Sparks, "Sediments of the Mississippi, Alabama, and Florida (MAFLA) continental shelf," *J. Sed. Pet.*, vol. 50, pp. 905–916, 1980.

[27] S. D. Locker and L. J. Doyle, "Neogene to recent stratigraphy and depositional regimes of the northwest Florida inner continental shelf," *Mar. Geol.*, vol. 104, pp. 123–138, 1992.

[28] P. Fleischer, W. B. Sawyer, H. Fiedler, and I. H. Stender, "Spatial and temporal variability of a coarse-sand anomaly on a sandy inner shelf, northeast Gulf of Mexico," *Geo-Mar. Lett.*, vol. 16, pp. 166–172, 1996.

[29] R. A. McBride, "Seafloor morphology, geologic framework, and processes of a sand-rich shelf offshore Alabama and Northwest Florida: Northeastern Gulf of Mexico," PhD, Dept. of Oceanography and Coastal Sciences, Louisiana State Univ., Baton Rouge, LA, 1997.

[30] K. R. Dryer and D. A. Huntley, "The origin, classification and modeling of sand banks and ridges," *Continental Shelf Res.*, vol. 19, pp. 1285–1330, 1999.

[31] S. D. Locker, K. D. Logue, and L. J. Doyle, "Neogene stratigraphy, bedforms and surface sediments: NW Florida state waters," The Center for Nearshore Marine Science, Univ. of South Florida, St. Petersburg, FL, 1988.

[32] J. F. Donoghue, "Late Wisconsinan and Holocene depositional history, northeastern Gulf of Mexico," *Mar. Geol.*, vol. 112, pp. 185–205, 1993.

[33] G. W. Stone and F. W. Stapor, "A nearshore sediment transport model for the northeast Gulf of Mexico Coast, U.S.A," *J. Coastal Res.*, vol. 12, pp. 786–792, 1996.

[34] J. V. Gardner, P. B. Butman, L. A. Mayer, and J. H. Clarke, "Mapping US continental shelves," *Sea Technol.*, vol. 39, no. 6, pp. 10–17, 1998.

[35] J. E. H. Clarke, L. A. Mayer, and D. E. Wells, "Shallow-water imaging multibeam sonars: A new tool for investigating seafloor processes in the coastal zone and on the continental shelf," *Mar. Geophys. Res.*, vol. 18, pp. 607–629, 1996.

[36] S. G. Schock and H. G. Herrmann, "Acoustic classification of subsurface sediment layers using multi-feature pattern recognition and least squares inversion," *Ocean Commun. Conf.*, vol. 98, Nov 17 1998.

[37] W. W. Schroeder, S. P. Dinnel, F. J. Kelly, and W. J. Wiseman Jr, "Overview of the physical oceanography of the Louisiana-Mississippi-Alabama continental shelf," in *Northeastern Gulf of Mexico Physical Oceanography Workshop: Florida State University*. ser. OCS Study MMS 94–0044, A. J. Clark, Ed. New Orleans, LA: Dept. of the Interior, Minerals Management Service, 1994, pp. 13–16.

[38] A. J. Clarke, "Overview of the physical oceanography of the Florida shelf in the study region," in *Northeastern Gulf of Mexico Physical Oceanography Workshop: Florida State University*. ser. OCS Study MMS 94–0044, A. J. Clark, Ed. New Orleans, LA: Dept. of the Interior, Minerals Management Service, 1994, pp. 17–36.

[39] W. W. Schroder, S. P. Dinnel, W. W. Wiseman, and W. J. Merrell, "Circulation papers inferred from the movement of detached buoys in the eastern Gulf of Mexico," *Continental Shelf Res.*, vol. 7, pp. 883–894, 1989.

[40] O. K. Huh, L. J. Rouse, and N. D. Walker, "Cold-air outbreaks over the northwest Florida continental shelf: heat flux processes and hydrographic changes," *J. Geophys. Res.*, vol. 89, pp. 717–726, 1984.

[41] C. P. Moeller, O. K. Huh, H. H. Roberts, L. E. Gumley, and W. P. Menzel, "Response of Louisiana coastal environments to a cold front passage," *J. Coastal Res.*, vol. 9, pp. 434–447, 1993.

[42] S. P. Murray, "Bottom currents near the coast during Hurricane Camille," *J. Geophys. Res.*, vol. 75, pp. 4579–4582, 1970.

[43] P. H. Dahl, "On bistatic sea surface scattering: Field measurements and modeling," *J. Acoust. Soc. Amer.*, vol. 105, no. 4, pp. 2155–2169, 1999.

[44] R. Soulsby, *Dynamic of marine sands*, U.K.: Thomas Telford Publications, 1997, p. 249.

[45] K. B. Briggs and R. I. Ray, "Seafloor roughness power spectra: trends and implications for high-frequency acoustic modeling," in *Shallow Water Acoustics*, R. Zhang and J. Zhou, Eds. Beijing, China: China Ocean Press, 1997, pp. 347–352.

[46] A. P. Lyons, W. L. J. Fox, T. Hasiotis, and E. Pouliquen, "Characterization of the two-dimensional roughness of shallow-water sandy seafloors," *IEEE J. Oceanic Eng.*, to be published.

[47] K. B. Atkinson, *Close Range Photogrammetry and Machine Vision*. Caithness, Scotland: Whittles Publishing, 1996.

[48] B. H. Jahne, Haussecker, and P. Geissler, *Handbook of Computer Vision and Applications*. San Diego, CA: Academic, 1999.

[49] K. B. Briggs, "High-frequency acoustic scattering from sediment interface roughness and volume inhomogeneities," Ph.D, Univ. of Miami, Coral Gables, FL, 1994.

[50] M. D. Richardson and K. B. Briggs, "On the use of acoustic impedance values to determine sediment properties," in *Acoustic Classification and Mapping of The Seabed*, N. G. Pace and D. N. Langhorne, Eds, U.K.: Institute of Acoustics, University of Bath, 1993, pp. 15–25.

[51] C. S. Martens, D. B. Albert, and M. J. Alperin, "Biogeochemical processes controlling methane in gassy coastal sediments – Part 1: A model coupling organic matter flux to gas production, oxidation and transport," *Continental Shelf Res.*, vol. 18, pp. 1741–1770, 1998.

[52] D. B. Albert, C. S. Martens, and M. J. Alperin, "Biogeochemical processes controlling methane in gassy coastal sediments – Part 2: groundwater flow control of acoustic turbidity in Eckernförde Bay Sediments," *Continental Shelf Res.*, vol. 18, pp. 1771–1793, 1998.

[53] M. D. Richardson, "Attenuation of shear waves in near-surface sediments," in *High-Frequency Acoustics in Shallow Water*, N. G. Pace, E. Pouliquen, O. Bergem, and A. P. Lyons, Eds. La Spezia, Italy, 1997, SACLANTCEN, pp. 451–457.

[54] ——, "In-situ, shallow-water sediments geoacoustic properties," in *Shallow-Water Acoustics*, R. Zang and J. Zhou, Eds. Beijing, China: China Ocean Press, 1997, pp. 163–170.

[55] P. D. Jackson, D. Taylor-Smith, and P. N. Stanford, "Resistivity-particle shape relationships for marine sands," *Geophysics*, vol. 43, pp. 1250–1268, 1978.

[56] R. D. Stoll, "New tools for studying seafloor geotechnical and geoacoustic properties," *J Acoust. Soc. Amer.*, vol. 66, pp. 2937–2944, 1994.

[57] R. D. Stoll, G. M. Bryan, and E. Bautista, "Masuring lateral variability of sediment geoacoustic properties," *J. Acoust. Soc. Amer.*, vol. 96, pp. 427–438, 1994.

[58] L. D. Bibee and L. M. Dorman *et al.*, "Full waveform inversion of seismic interface wave data," in *Full Field Inversion Methods in Ocean and Seismo-Acoustics*, O. Diachok *et al.*, Eds. Dordrecht, The Netherlands: Kluwer, 1995.

[59] H. L. Hamilton, "Shear wave velocity versus depth in marine sediments: A review," *Geophysics*, vol. 68, pp. 985–996, 1976.

[60] G. B. Deane, M. J. Buckingham, and C. T. Tindle, "Vertical coherence of ambient noise in shallow water overlying a fluid seabed," *J. Acoust. Soc. Amer.*, vol. 102, pp. 3413–3424, 1997.

[61] O. A. Godin, N. R. Chapman, M. C. A. Laidlaw, and D. E. Hannay, "Head wave data inversion for geoacoustic parameters of the ocean bottom off Vancouver Island," *J. Acoust. Soc. Amer.*, vol. 106, pp. 2540–2551, 1999.

[62] R. H. Bennett, H. Li, D. N. Lambert, K. M. Fischer, D. J. Walter, C. E. D. J. Hickox, M. H. Hulbert, T. Yamamoto, and M. Badiey, "In situ porosity and permeability of selected carbonate sediment: Great Bahama Bank Part 1: Measurements," *Mar. Geotechnol.*, vol. 9, pp. 1–28, 1989.

[63] W. E. Brown and H. W. Patnode, "Plastic lithification of sands in situ," *AAPG Bull.*, vol. 37, pp. 152–157, 1953.

[64] A. P. Lyons and T. H. Orsi, "The effect of a layer of varying density on high-frequency reflection, forward loss and backscatter," *IEEE J. Oceanic Eng.*, vol. 23, pp. 411–422, 1998.

[65] D. Tang and T. H. Orsi, "Three-dimensional density spectra of sandy sediments," J. Acoust. Soc. Amer., vol. 107, pp. 1953–1965, 2000, to be published.

[66] T. H. Orsi, "Computed tomography of macrostructure and physical property variability of seafloor sediments," Ph.D, Texas A&M Univ., College Station, TX, 1994.

[67] T. H. Orsi and A. L. Anderson, "Bulk density calibration for X-ray tomographic analyzes of marine sediments," *Geo-Mar. Lett.*, vol. 19, pp. 270–274, 1999.
[68] A. L. Alldredge and J. M. King, "Effects of moonlight on the vertical migration patterns of demersal zooplankton," *J. Exp. Mar. Biol. Ecol.*, vol. 44, pp. 133–156, 1980.
[69] J. Mauchline, "The biology of mysids and euphausids," in *Advances in Marine Biology*, J. H. S. Blaxter, F. S. Russell, and M. Yonge, Eds. New York: Academic, 1980, vol. 18.
[70] J. W. Deming and R. R. Colwell, "Barophilic bacteria associated with digestive tracts of abyssal holothurians," *Appl. Environ. Microbiol*, vol. 44, pp. 1222–1230, 1982.
[71] S. S. Epstein and J. Rossel, "Enumeration of sandy sediment bacteria: search for optimal protocol," *Mar. Ecol. Prog. Ser.*, vol. 117, pp. 289–298, 1995.
[72] J. L. Schmidt, J. W. Deming, P. A. Jumars, and R. G. Keil, "Constancy of bacterial abundance in surficial marine sediments," *Limnol. Oceanogr.*, vol. 43, pp. 976–982, 1998.
[73] J. C. Russ, *Practical Stereology*. New York, NY: Plenum, 1986, p. 194.
[74] L. M. Mayer, "Surface area control of organic carbon accumulation in continental shelf sediments," *Geochim. Cosmochim. Acta*, vol. 58, pp. 1271–1284, 1994.

Michael D. Richardson received the B.S. degree in oceanography from the University of Washington, Seattle, in 1967, the M.S. degree in marine science from the College of William and Mary, Williamsburg, VA, in 1971, and the Ph.D. degree in oceanography in 1976.

He began working at the Naval Research and Development Activity, now part of the Naval Research Laboratory (NRL), Stennis Space Center, MS, in 1977. Except for a five-year assignment as Principle Scientist at NATO's SACLANTCEN, La Spezia, Italy (1985–1989), he has worked at NRL as a Research Scientist and is currently head of the Seafloor Sciences Branch in the Marine Geosciences Division. His research interests include the effects of biological and physical processes on sediment structure, behavior, and physical properties near the sediment–water interface in both shallow-water coastal regions and in the deep sea. His current research is linked to high-frequency acoustic scattering from and propagation within the seafloor and prediction of mine burial.

Dr. Richardson is a member of the Acoustical Society of America, the American Geophysical Union, the European Geophysical Society, and Sigma Xi.

Due to space constraints, the remaining authors will not be listed.